# Page Proof Instructions and Queries

**Journal Title:** PID
**Article Number:** 1021207

Thank you for choosing to publish with us. This is your final opportunity to ensure your article will be accurate at publication. Please review your proof carefully and respond to the queries using the circled tools in the image below, which are available in Adobe Reader DC* by clicking **Tools** from the top menu, then clicking **Comment**.

Please use *only* the tools circled in the image, as edits via other tools/methods can be lost during file conversion. For comments, questions, or formatting requests, please use T. Please do *not* use comment bubbles/sticky notes.

*If you do not see these tools, please ensure you have opened this file with **Adobe Reader DC**, available for free at get.adobe.com/reader or by going to Help >Check for Updates within other versions of Reader. For more detailed instructions, please see us.sagepub.com/ReaderXProofs.

| Sl. No. | Query |
|---|---|
| | Please note that we cannot add/amend orcid ids for any article at the proof stage. following orcid's guidelines, the publisher can include only orcid ids that the authors have specifically validated for each manuscript prior to official acceptance for publication. |
| | Please confirm that all author information, including names, affiliations, sequence, and contact details, is correct. |
| | Please review the entire document for typographical errors, mathematical errors, and any other necessary corrections; check headings, tables, and figures. |
| | Please ensure that you have obtained and enclosed all necessary permissions for the reproduction of art works (e.g. illustrations, photographs, charts, maps, other visual material, etc.) not owned by yourself. please refer to your publishing agreement for further information. |
| | Please note that this proof represents your final opportunity to review your article prior to publication, so please do send all of your changes now. |
| | Please confirm that the funding and conflict of interest statements are accurate. |
| 1 | Figure 12 citation is missing, please check and provide. |
| 2 | Please provide the editors name, publisher and location for the reference 1. |
| 3 | Please provide the accessed date for the reference 3. |
| 4 | Please provide the publisher location for the reference 4. |
| 5 | Please provide the publisher location for the reference 12. |
| 6 | Please provide the conference location for the reference 14. |
| 7 | Please provide the conference location for the reference 17. |
| 8 | Please provide the location for the reference 19. |
| 9 | Please provide the publisher location for the reference 20. |
| 10 | Please provide the updated information for the reference 21. |
| 11 | Please provide the conference location for the reference 24. |
| 12 | Please provide the location for the reference 29. |
| 13 | Please provide the conference location for the reference 31. |
| 14 | Please provide the conference location for the reference 34. |

Original Article

Institution of MECHANICAL ENGINEERS
Journal of AUTOMOBILE ENGINEERING

Proc IMechE Part D:
J Automobile Engineering
1–19
© IMechE 2021
Article reuse guidelines:
sagepub.com/journals-permissions
DOI: 10.1177/09544070211021207
journals.sagepub.com/home/pid
SAGE

# Physics-based linear model predictive control strategy for three-way catalyst air/fuel ratio control

**Abdullah-al Mamun[1], Qilun Zhu[1], Mark Hoffman[2] and Simona Onori[1,3]**

**Abstract**

Current practice of air-fuel ratio control relies on empirical models and traditional PID controllers which require extensive calibration to maintain the post-catalyst air-fuel ratio close to stoichiometry. In contrast, this work utilizes a physics-based Three-Way Catalyst (TWC) model to develop a model predictive control (MPC) strategy for air-fuel ratio control based on internal TWC oxygen storage dynamics. In this paper, parameters of the physics-based temperature and oxygen storage models of the TWC are identified using vehicle test data for a catalyst aged to 150,000 miles. A linearized oxygen storage model is then developed from the identified nonlinear model, which it is shown, in simulation, to follow the nonlinear model with minimal error during nominal operation. This motivates the development of a Linear MPC (LMPC) framework using the linearized TWC oxygen storage model, reducing the requisite computational effort relative to a nonlinear MPC strategy. In this work, the LMPC utilizing a linearized physics-based TWC model is proven suitable for tracking a desired oxygen storage level by controlling the commanded engine air-fuel ratio, which is also a novel contribution. The offline simulation results show successful tracking performance of the developed LMPC framework.

**Keywords**

Three-way catalyst, model predictive control, air-fuel ratio control, physics-based model, oxygen storage level

Date received: 25 October 2020; accepted: 19 March 2021

## Introduction

Ongoing efforts to reduce harmful fossil fuel emissions in conjunction with ever tightening emission standards have stimulated great interest in improved emission control strategies.[1–3] In a Three-Way Catalyst (TWC), unburned hydrocarbons and carbon monoxide in the exhaust gas are converted to carbon dioxide while oxides of nitrogen are converted to nitrogen gas. TWC conversion efficiency critically depends on the quantity of stored oxygen, which, in turn, changes based on the exhaust gas air-fuel ratio.[4] To simultaneously facilitate both oxidation and reduction reactions, the TWC cannot be completely saturated with or devoid of oxygen. Conventional feedback control strategies alter engine air-fuel ratio based on estimates of the gaseous oxygen quantity downstream of TWC. In contrast, directly utilizing the TWC oxygen storage level within the air-fuel ratio control strategy promises to deliver higher exhaust gas conversion efficiencies.

In the automotive industry, the common practice is to dither the pre-catalyst air-fuel ratio near stoichiometry. A feedforward-feedback controller is generally implemented where pre and post-catalyst lambda measurements are used to correct the air-fuel ratio signal computed from the feedforward path.[5,6] A wide body of literature has focused on developing control strategies to maintain the air-fuel ratio close to stoichiometry while compensating for disturbances and delays in the system.[7–11] Even though the current control techniques work well in most cases, they require extensive calibration of the feedforward and feedback controllers for effective emissions mitigation.

Unfortunately, the pollution conversion efficiency as a function of the pre-catalyst air-fuel ratio only

[1]Department of Automotive Engineering, Clemson University, Greenville, SC, USA
[2]Department of Mechanical Engineering, Auburn University, Auburn, AL, USA
[3]Department of Energy Resources Engineering, Stanford University, Stanford, CA, USA

**Corresponding author:**
Simona Onori, Department of Energy Resources Engineering, Stanford University, Panama Mall, Stanford, CA 94305, USA.
Email: sonori@stanford.edu

represents the steady-state behavior of the catalyst. Transient TWC behavior is dominated by the slow dynamics of oxygen storage and release,[12] altering the conversion efficiency even though the upstream lambda value remains constant. Therefore, for emission control, it is more important to track a desired TWC oxygen storage level rather than tracking pre and post-catalyst air-fuel ratio.[6] A TWC model with oxygen storage dynamics would facilitate such model-based TWC control. Additionally, during highly dynamic operation, air and fuel disturbances caused by intake manifold wave dynamics and wall-wetting, respectively, cause disturbances to air-fuel ratio tracking.[13] Thus, temporary air-fuel ratio excursions are possible even in a well-calibrated system. Through TWC oxygen storage level tracking, such excursions can be effectively damped, resulting in higher conversion efficiency.

Another important factor for TWC control is rewetting after a fuel cut-off event. During a fuel cutoff, the TWC becomes saturated with oxygen. In current calibration-based control efforts, the TWC oxygen level is intentionally depleted after the cut-off event by enriching the air-fuel ratio command, which consumes excess fuel.[12] Maintaining a steady TWC oxygen storage level through active tracking of a oxygen storage reference has the potential to reduce rich TWC re-wetting. Therefore, a model-based control approach that takes into account the system states, such as oxygen storage level, can lead to increased conversion of the harmful exhaust species in the TWC. Reduced breakthrough of harmful emission species using a model-based control approach might also facilitate a TWC size reduction or even the elimination of a secondary TWC brick, reducing the capital cost of the aftertreatment system. Different model-based control techniques utilizing estimated oxygen storage level are used for TWC emission control.

A combined PID controller and Linear Quadratic Regulator (LQR) scheme is proposed in Tomforde et al.[6] where the PID controller keeps the pre-catalyst air-fuel ratio close to a desired setpoint and the post-catalyst LQR corrects that setpoint based on the estimated TWC oxygen storage level. The spatial distribution of oxygen storage level is modeled by connecting multiple cells in series where the oxygen storage level of each cell depends empirically on mass flow rate and air-fuel ratio only. A similar cascade controller is developed in Balenovic and Backx[14] where an Internal Model Controller (IMC) for engine air-fuel ratio control is placed in the inner loop and a proportional feedback TWC controller is placed in the outer loop. The proportional feedback controller is tuned to keep the relative oxygen level at a desired value determined from a control oriented empirical storage model. Later, this work was extended by replacing the outer TWC feedback controller with a neural network trained from offline nonlinear MPC solution.[15] A similar approach is presented in Muske and Jones[16] to minimize emissions as well as fuel consumption. In this case, feedback is provided by a moving horizon oxygen storage level estimation scheme, and the control action is calibrated based on the offline solution of a nonlinear MPC. In Mallik,[17] a state feedback controller and an adaptively tuned PID controller are developed to maintain a reference oxygen storage level. Finally in Trimboli et al.[18] a model predictive controller is developed and MPC feedback laws are computed as piecewise affine functions for online implementation.

Clearly, empirical oxygen storage models similar to Brandt et al.[19] and Guzzella and Onder[20] are commonly utilized for TWC air-fuel ratio control. However, such lumped empirical models not only neglect the spatial non-uniformity of TWC oxygen level but also unable to maintain their accuracy as the catalyst ages. In contrast, a physics-based TWC model takes into account the underlying physical processes, such as heat-transfer, chemical kinetics, and fluid dynamics. Additionally, physical models include oxygen storage capacity, a quantity that can be related to TWC performance degradation over time. Therefore, such a physics-based model enables improved air-fuel ratio control over the lifetime of the TWC through proper oxygen storage level estimation.

From the above literature, it is evident that offline MPC is often used to extract rule-based air-fuel ratio control strategies for TWC. The practice of extracting such rules from offline MPC stems from the computational complexity of the nonlinear TWC oxygen storage dynamics model in the MPC framework. Inclusion of spatial oxygen storage level variations via a physics-based TWC model would further increase the computational load of air-fuel ratio control using a nonlinear MPC. Therefore, a computationally efficient online MPC algorithm is needed for tracking a non-uniform distribution of oxygen storage level in a TWC, which is still missing in the literature. This paper fills that void by developing an LMPC strategy using a linearized, physics-based TWC oxygen storage model. The avoidance of nonlinear MPC reduces the computational load, making it possible to implement the proposed TWC control strategy within ever advancing ECUs. LMPC is widely accepted by the industry for its computational efficiency, and well-developed stability theories.[21] Current micro-processors, including ECUs, are fast enough to solve quadratic Programming (QP) problems in milliseconds using active set[22] or interior point QP algorithms.[23] This technology evolution enables the application of real-time MPC in systems with fast dynamics to find optimal transient control actions.[24] In Bemporad,[25] the first instance of MPC developement is found for production engine control units.

This work utilizes existing 1-D, physics-based temperature and oxygen storage model of a TWC and spatially discretizes temperature and oxygen storage level along the length of the TWC.[26] The TWC oxygen storage and thermal model parameters are identified for an aged catalyst. Subsequently, an observer is built around

the model to estimate the nonuniform axial distribution of oxygen storage level from sensor measurements. A LMPC controller is then developed to track reference oxygen storage levels in each discretized zone within the TWC. To implement the LMPC, a linearized version of the 1-D, physics-based, TWC oxygen storage model is developed. The accuracy of the linearized and nonlinear oxygen storage level models is thoroughly examined for different time steps and lengths of MPC prediction horizon. A simulation study shows that the proposed LMPC framework can successfully track the desired TWC oxygen storage level during transient drive cycles.

Future extension of this research will validate the proposed TWC control strategy experimentally study the robustness of the proposed control against modeling error and measurement noise.

The remainder of this work is organized as follows. Section 2 describes the chemical processes inside a TWC. A nonlinear physics-based TWC model, model parameter identification, and linearized TWC model are presented in Section 3. Sections 4 and 5 outline the formulation and the implementation of the linear MPC, respectively. Section 6 presents the characterization of engine delay dynamics for future in-vehicle implementation of the proposed controller, and Section 7 summarizes the conclusions.

## Three-way catalyst device

A TWC is an exhaust gas aftertreatment device that mitigates emission of harmful gases such as nitrogen oxide, carbon monoxide, and hydrocarbons by converting them into nitrogen, carbon dioxide, and water as shown in (1).[27] The TWC has a substrate with narrow channels through which the exhaust gas flows. The surface of the substrate is covered with a washcoat containing alumina oxide, cerium oxide, a mixture of precious metals, and stabilizers.[12]

$$\begin{aligned} C_xH_y + (x + \frac{y}{4})O_2 &\rightarrow xCO_2 + \frac{y}{2}H_2O \\ CO + \frac{1}{2}O_2 &\rightarrow CO_2 \\ NO_x &\rightarrow \frac{1}{2}N_2 + \frac{x}{2}O_2 \end{aligned} \tag{1}$$

Conversion efficiency of these species depends on the air-fuel ratio, $A/F$, defined as the ratio of air mass ($m_{air}$) to the fuel mass ($m_{fuel}$) in the exhaust gas. The exhaust gas entering the TWC is quantified using the normalized air-fuel ratio, $\lambda$, defined as follows:

$$\lambda = \frac{(A/F)_{actual}}{(A/F)_{stoich}} \tag{2}$$

where, $(A/F)_{stoich}$ denotes the air-fuel ratio required for complete combustion of the fuel which is 14.7 for gasoline engines. In (2), $(A/F)_{actual}$ is the actual air-fuel ratio of the exhaust gas defined as:

$$(A/F)_{actual} = \frac{m_{air}}{m_{fuel}} \tag{3}$$

As shown in Figure 1, the conversion efficiency of the pollutants reaches its maximum near stoichiometry, $\lambda = 1$. $\lambda > 1$ corresponds to lean operation (excess air compared to stoichiometry) while $\lambda < 1$ corresponds to rich operation (excess fuel compared to stoichiometry).[20] Lack of oxygen during rich operation affects the conversion efficiency of carbon monoxide and hydrocarbons. In contrast, excess oxygen during lean operation prevents reduction of nitrogen oxide. To maintain a window of opportunity for high conversion efficiency, cerium oxide ($Ce_2O_4$) and precious metals are added in the washcoat of the catalyst.[28] During transient vehicle operation, the pre-catalyst normalized air-fuel ratio, $\lambda_{pre}$, fluctuates significantly. The washcoat allows temporary storage and release of oxygen to maintain a lambda value close to unity. The oxygen storage level needs to be controlled to keep the conversion rate high during vehicle operation.

## TWC physics-based model

To model the dynamic TWC behavior, a nonlinear temperature and oxygen storage model are obtained from Sabatini et al.[26] The temperature model computes the brick temperature at different axial locations within the catalyst for a given exhaust mass flow rate, $\dot{m}_{exh}$, and exhaust gas temperature, $T_{exh}$. The brick temperature, $T_{cat,mid}$, calculated at the mid point of the brick is then used as a time varying parameter in the oxygen storage model. The oxygen storage model estimates the amount of oxygen stored at different axial locations of the catalyst at each time instant for a given $\lambda_{pre}$, $T_{exh}$, and $\dot{m}_{exh}$. In the following subsection, the temperature and oxygen storage model of TWC from Sabatini et al.[26] are summarized.

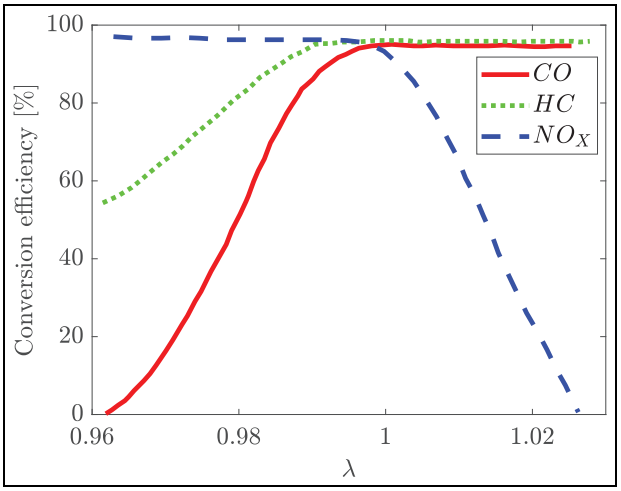


**Figure 1.** Variation of pollutant species conversion efficiency versus normalized air-fuel ratio, $\lambda$ (figure reproduced from Sabatini et al.[26]).

### Temperature model

The partial differential equation (PDE) based TWC temperature model presented in Sabatini et al.[29] is used in this work to capture the gas and solid phase temperature dynamics inside the catalyst:

$$\frac{\dot{m}_{exh}}{A_{CS}} c_{p_g} \frac{\partial T_g}{\partial z} = hA_{geo}(T_{cat} - T_g) \tag{4}$$

$$\rho_s(1-\epsilon)c_s \frac{\partial T_{cat}}{\partial t} = (1-\epsilon)\lambda_s \frac{\partial^2 T_{cat}}{\partial z^2} - hA_{geo}(T_{cat} - T_g) + \dot{Q}_{reac} - \frac{A_{out}}{V_{cat}} h_{out}(T_{cat} - T_{amb}) \tag{5}$$

where, $c_{p_g}$, $\dot{m}_{exh}$, $T_g$, $T_{cat}$, $\rho_s$, $c_s$, $\epsilon$, $T_{amb}$, and $\dot{Q}_{reac}$ are the specific heat of the exhaust gas, exhaust mass flow rate, exhaust gas temperature, catalyst temperature, TWC solid phase density, TWC solid phase specific heat, TWC open cross sectional area, ambient temperature, and heat generation due to chemical reactions, respectively. Since modeling the heat generation from chemical kinetics is computationally expensive, the simplified heat generation model used in this paper expresses the chemical heat generation rate, $\dot{Q}_{reac}$ by a hyperbolic tangent function, which is dependent on the exhaust mass flow rate, catalyst solid phase temperature, and catalyst light-off temperature as follows[30]:

$$\dot{Q}_{reac} = 0.5K_{reac}\dot{m}_{exh}tanh[a(T_{cat} - T_{light-off})] + 0.5 \tag{6}$$

where, $K_{reac}$, $a$, $T_{light-off}$ are a proportional constant, the slope of the hyperbolic tangent function, and the light-off temperature, respectively.

### Oxygen storage model

Most of the TWC oxygen storage can be attributed to cerium oxide ($Ce_2O_4$), also known as ceria, in the washcoat. The oxygen absorption and release in ceria are modeled by the following reactions:

$$O_2 + 2Ce_2O_3 \leftrightarrow 2 \cdot Ce_2O_4 \tag{7a}$$

$$CO + 2Ce_2O_4 \leftrightarrow CO_2 + Ce_2O_3 \tag{7b}$$

The rate of the above oxygen absorption and release reaction determine the rate of change in the TWC oxygen storage level. The oxygen storage level, $\phi$, is a normalized quantity describing the ratio of the stored oxygen in a TWC (i.e. the concentration of $[Ce_2O_4]$) to the maximum amount of oxygen that the TWC can store. The maximum amount of oxygen that a TWC can store, is defined as the oxygen storage capacity, $OSC$ (in $mol/m^3$). $OSC$ is the sum of the cerium (IV) oxide concentration, $[Ce_2O_4]$ that has already absorbed oxygen and the cerium (III) oxide concentration, $[Ce_2O_3]$ that is still available for oxygen absorption.

$$\phi = \frac{[Ce_2O_4]}{[Ce_2O_4] + [Ce_2O_3]} \tag{8}$$

The spatially discretized TWC thermal model with five cells and oxygen storage model with three cells provided in Sabatini et al.[26] are used in this paper for subsequent analysis. In each cell of the thermal model, uniform TWC temperature is assumed and similarly, in each cell of the oxygen storage model, uniform oxygen storage level is assumed. The catalyst temperature computed at the TWC midpoint by the temperature model is used as an input to the oxygen storage model as shown in Figure 2. Throughout the rest of the paper, the temperature at the axial centerpoint location of the TWC brick is denoted as $T_{cat,mid}$. The oxygen storage level at $j$ th cell from the inlet of the TWC is expressed as Sabatini et al.[26]:

$$\begin{aligned}\frac{\partial \phi^j}{\partial t} = \frac{1}{OSC}[&2(A_1 e^{-\frac{E_1}{R_u T_{cat,mid}}}(OSC \cdot (1-\phi^j))^2[O_2]^j \\ &- A_1 e^{\frac{\Delta G_1 - E_1}{R_u T_{cat,mid}}}(OSC \cdot \phi^j)^2 c_o) \\ &- (A_2 e^{-\frac{E_2}{R_u T_{cat}}}(OSC \cdot \phi^j)[CO]^j \\ &- A_2 e^{\frac{\Delta G_2 - E_2}{R_u T_{cat,mid}}}(OSC \cdot (1-\phi^j))[CO_2]^j)]\end{aligned} \tag{9}$$

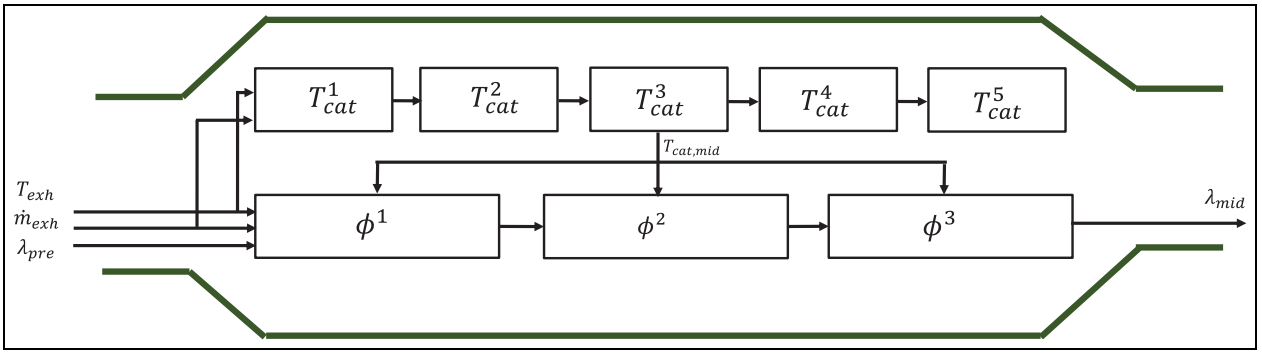


**Figure 2.** The input, outputs, and spatial discretization of the temperature model and the oxygen storage model of a TWC. The nonlinear temperature model is run in open loop fed by the exhaust gas temperature and exhaust gas mass flow rate which output the mid brick temperature ($T_{cat,mid}$). The inputs to the oxygen storage model are the exhaust gas temperature, exhaust mass flow rate, and pre-catalyst normalized air-fuel ratio and output is the normalized air-fuel ratio after the first brick.

With the concentration of species at the inlet as initial conditions, the concentration of species at cell $j$ are obtained where $[O_2]^j = f_{O_2}([O_2]^{j-1}, \phi^j)$, $[CO]^j = f_{CO}([CO]^{j-1}, \phi^j)$, $[CO_2]^j = f_{CO_2}([CO_2]^{j-1}, \phi^j)$. For control developement purposes, we use three discretized cells, that is, $j = 1, 2, 3$, whereas for identification we use 40 discretized cells.

### Normalized air-fuel ratio

The pre-catalyst normalized air-fuel ratio, $\lambda_{pre}$, is an input to the oxygen storage model. Given $\lambda_{pre}$, the species concentration at the TWC inlet are determined by Kiwitz et al.[27]:

$$\begin{aligned}
[O_2] &= \max([O_2]_{stoich}, (\lambda_{pre} - \frac{1}{2})[CO]_{stoich} \\
&\quad + (\lambda_{pre} - 1)[CO_2]_{stoich}) \\
[CO] &= \max([CO]_{stoich}, \\
&\quad \frac{[O_2]_{stoich} + (\lambda_{pre} - 1)[CO_2]_{stoich}}{\lambda_{pre} - \frac{1}{2}}) \\
[CO_2] &= 0.12 \cdot [CO_2]_{stoich}
\end{aligned} \tag{10}$$

The stoichiometric gas concentrations in (10) are obtained from Guzzella and Onder[20] as a function of the total exhaust gas concentration ($c_o$) as follows:

$$\begin{aligned}
[O_2]_{stoich} &= 1\% c_o \\
[CO]_{stoich} &= 2\% c_o \\
[CO_2]_{stoich} &= 12\% c_o
\end{aligned} \tag{11}$$

In this work, the normalized air-fuel ratio downstream of first brick is denoted as $\lambda_{mid}$. Given the concentration of $O_2$, $CO$, and $CO_2$ downstream of the brick, the normalized air-fuel ratio is computed as follows[20]:

$$\lambda_{mid} = \frac{2[O_2] + [CO] + 2[CO_2]}{2[CO] + 2[CO_2]} \tag{12}$$

### Model parameter identification

In this work, the temperature and oxygen storage model parameters are identified for a 150,000 mile aged TWC and utilized in the subsequent controller development. The experimental data for identification was gathered at the Department of Automotive Engineering, Clemson University. A 150,000 aged catalyst is mounted in a commercially available passenger vehicle, which is run on a Renk Labeco 500HP Chassis Dyno and subjected to various drive cycles. The normalized air-fuel ratio at the pre-catalyst and mid-catalyst locations are measured using wide band lambda sensors. The exhaust gas temperature and catalyst brick temperature are measured using type K thermocouples and the exhaust mass flow rate data is extracted from the vehicle ECU. For identification, a concatenated drive cycle is generated where the US06, FTP, and HWY test cycles are run back to back.

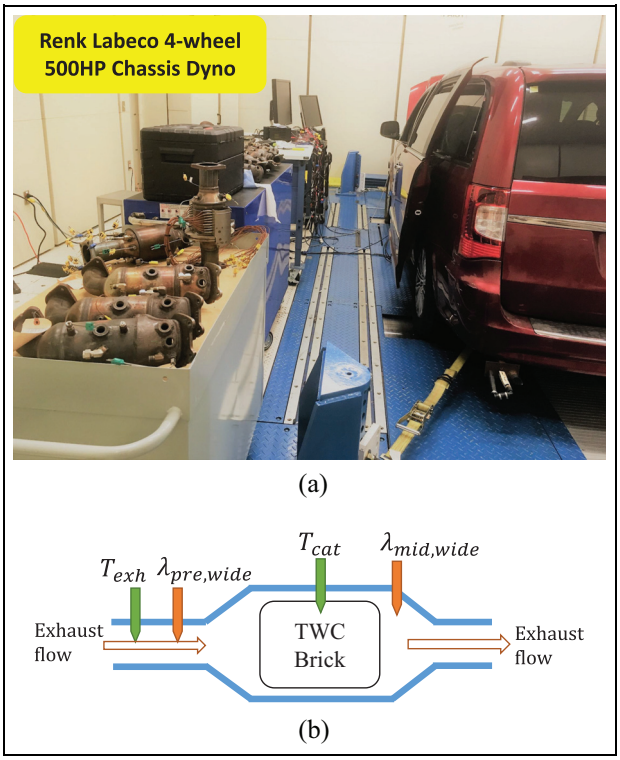


**Figure 3.** (a) The chassis-dyno and the experimental setup used for vehicle and TWC data collection at the Clemson University Department of Automotive Engineering, (b) schematic layout of the thermocouples and wide-band lambda sensors to measure the exhaust gas temperature, TWC brick temperature, and normalized air-fuel ratio before and after the first TWC brick.

Figure 3 shows the chassis-dyno setup used for testing and presents a schematic of the TWC sensor locations used during testing. Similar to Sabatini et al.[26] the fuel cut off portion of the signals were not used for identification. Reactivity is stymied during fuel cuts and excluded from the lean fuel cut data in the model identification.

First, the temperature model parameters are identified since they are independent of the oxygen storage dynamics and only depend on the mass flow rate and temperature of the exhaust gas. From (4)–(6) those are

$$\theta_T = [\rho_s \cdot c_s \quad h \quad h_{out} \quad K_{reac} \quad s \quad T_{light-off}] \tag{13}$$

The temperature model is discretized along the length of the TWC into 40 cells and simulated using the exhaust gas mass flow rate and exhaust temperature recorded during the chassis-dyno experiments and the brick temperature ($T_{cat}$) at each discrete cell is computed at each time step. Since the brick temperature is measured halfway along the length of the brick, the simulated brick temperature at the center location along the length of the brick is compared with the measurement. A particle swarm optimization (PSO) algorithm is used to minimize the root mean square error (RMSE) between measured and simulated brick temperatures, that is

**Table 1.** Identified parameters for a 150,000 miles aged catalyst.

| Parameter | Value |
|---|---|
| $\rho_s \cdot c_s$ | $5.295 \times 10^6$ |
| $h$ | 111.275 |
| $h_{out}$ | 14.2499 |
| $K_{reac}$ | $2.21 \times 10^8$ |
| $s$ | 0.0165 |
| $T_{light-off}$ | 410.86 |
| $A_1$ | $4.177 \times 10^8$ |
| $A_2$ | 120.762 |
| $E_1$ | $3.51 \times 10^4$ |
| $E_2$ | $4.215 \times 10^3$ |
| $a_{Ce_2O_4}$ | 3.5433 |
| $b_{Ce_2O_4}$ | $-3.62 \times 10^4$ |
| $c_{Ce_2O_4}$ | 0 |
| $OSC$ | 19.64 |

$$RMSE_T = \sqrt{\frac{\sum_{t=1}^{K} \left(T_{cat,mid,meas,t} - T_{cat,mid,sim,t}\right)^2}{K}} \tag{14}$$

where, $T_{cat,mid,meas,t}$, and $T_{cat,mid,sim,t}$ are the measured and simulated brick temperature at the center, respectively, at time step $t$, from 1 to $K$, where $K$ is the total number of time steps in the concatenated drive cycle. The model-predicted catalyst temperature is then used in the oxygen storage model to identify the following unknown parameters:

$$\theta_\phi = [A_1 \;\; A_2 \;\; E_1 \;\; E_2 \;\; a_{Ce_2O_4} \;\; b_{Ce_2O_4} \;\; c_{Ce_2O_4} \;\; OSC] \tag{15}$$

The identification of parameter vector $\theta_\phi$ is performed using PSO with a 40 spatial discretization cell along the oxygen storage level PDE dynamics. The oxygen storage model is simulated using $\lambda_{pre}$, $\dot{m}_{exh}$, $T_{exh}$, and $T_{cat}$ as inputs and normalized air-fuel ratio at mid location, $\lambda_{mid}$ is calculated from (12). The simulated output, $\lambda_{mid,sim,t}$ at each time step $t$ is compared with measured normalized air-fuel ratio at mid location, $\lambda_{mid,meas,t}$ and the following RMSE is minimized using PSO:

$$RMSE_\phi = \sqrt{\frac{\sum_{t=1}^{K} \left(\lambda_{mid,meas,t} - \lambda_{mid,sim,t}\right)^2}{K}} \tag{16}$$

Table 1 includes the identified parameters for the TWC aged to 150,000 miles. The identified temperature and oxygen storage model is validated using experimental data from a US06 drive cycle. Figure 4 presents the pre-catalyst normalized air-fuel ratio, exhaust mass flow rate, and exhaust gas temperature obtained while running the US06 drive cycle in the chassis-dyno. The experimental input profiles in Figure 4 are used to simulate the identified temperature and oxygen storage model. The brick temperature, $T_{cat,mid}$ and $\lambda_{mid}$ computed from the model are compared with the measured data. Figure 5 shows the validation results where the

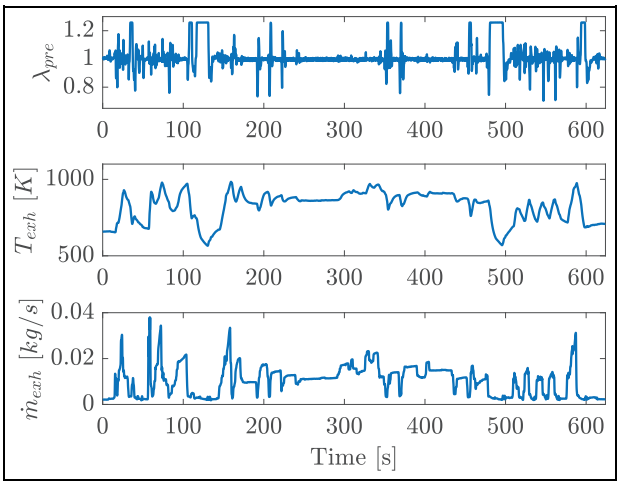


**Figure 4.** Experimental data set showing the pre-catalyst normalized air-fuel ratio, $\lambda_{pre}$, exhaust gas temperature, $T_{exh}$, and exhaust mass flow rate, $\dot{m}_{exh}$ during US06 drive cycle operation of the test vehicle in the chassis-dyno.

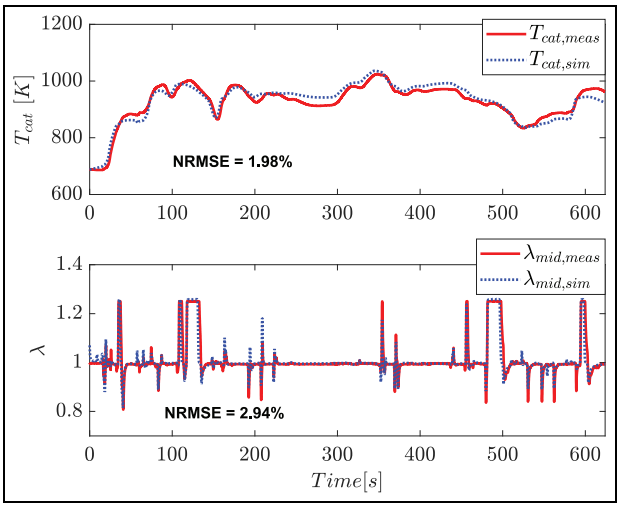


**Figure 5.** Validation of the simulated catalyst brick temperature and normalized air-fuel ratio after the first brick for a catalyst aged to 150,000 miles relative to the experimentally measured values while running the US06 drive cycle.

brick temperature $T_{cat,mid}$ and $\lambda_{mid}$ from the identified model are compared with the experimental data. The temperature model predicts the brick temperature with a normalized RMS error (NRMSE) of 1.98% with respect to the range of measured brick temperature. Similarly, the oxygen storage model predicts the $\lambda_{mid}$ value with a normalized RMS error of 2.94% with respect to the range of measured $\lambda_{mid}$.

## *Linearizion of the TWC oxygen storage model*

In this section, the linearization of the TWC oxygen storage model is carried out. The TWC states at time $t$ are represented by the state vector $\mathbf{x}(t) =$

$[\phi_1(t) \quad \phi_2(t) \quad \phi_3(t)]^T$ where $\mathbf{x} \in \mathbb{R}^{\mathbf{3}}_{[\mathbf{0},\mathbf{1}]}$. Given the exhaust gas temperature and mass flow rate, the TWC brick temperature at each time step is computed using (4)–(6) and provided to the oxygen storage model in (9) as a time varying parameter. The control variable in the oxygen storage model is the pre-catalyst air-fuel ratio $\lambda_{pre}$, whereas the exhaust temperature $T_{exh}$ and exhaust mass flow rate $\dot{m}_{exh}$ are considered as disturbances to the model. With $u(t) = \lambda_{pre}(t)$ as the model input and $\mathbf{w}(t) = [T_{exh}(t) \quad \dot{m}_{exh}(t)]^T$ as the disturbance vector, the control-oriented TWC dynamic model can be expressed as follows:

$$\dot{\mathbf{x}}(t) = f(\mathbf{x}(t), u(t), \mathbf{w}(t)) \tag{17}$$

At a given state, input, and disturbance operating point, $(\mathbf{x}_o, u_o, \mathbf{w}_o)$ from Taylor series expansion in (17), the following linearized model is obtained:

$$\begin{aligned}\dot{\mathbf{x}}(t) &= f_o(\mathbf{x}_o, u_o, \mathbf{w}_o) + \mathbf{A}(\mathbf{x}(t) - \mathbf{x}_o) \\ &\quad + \mathbf{B_u}(u(t) - u_o) + \mathbf{B_w}(\mathbf{w}(t) - \mathbf{w}_o)\end{aligned} \tag{18}$$

where the linearized state, input, and disturbance matrices $\mathbf{A}$, $\mathbf{B_u}$, and $\mathbf{B_w}$ are such that $\mathbf{A} \in \mathbb{R}^{\mathbf{3\times3}}$, $\mathbf{B_u} \in \mathbb{R}^{\mathbf{3\times1}}$, and $\mathbf{B_w} \in \mathbb{R}^{\mathbf{3\times2}}$, respectively, and are found from numerical perturbation as follows:

$$\begin{aligned}\mathbf{A} &= [\frac{\partial f}{\partial \mathbf{x}}]_{\mathbf{x}_o, u_o, \mathbf{w}_o} = \frac{f(\mathbf{x}_o + \delta\mathbf{x}, u_o, \mathbf{w}_o) - f(\mathbf{x}_o, u_o, \mathbf{w}_o)}{\delta\mathbf{x}} \\ \mathbf{B_u} &= [\frac{\partial f}{\partial u}]_{\mathbf{x}_o, u_o, \mathbf{w}_o} = \frac{f(\mathbf{x}_o, u_o + \delta u, \mathbf{w}_o) - f(\mathbf{x}_o, u_o, \mathbf{w}_o)}{\delta u} \\ \mathbf{B_w} &= [\frac{\partial f}{\partial \mathbf{w}}]_{\mathbf{x}_o, u_o, \mathbf{w}_o} = \frac{f(\mathbf{x}_o, u_o, \mathbf{w}_o + \delta\mathbf{w}) - f(\mathbf{x}_o, u_o, \mathbf{w}_o)}{\delta\mathbf{w}}\end{aligned} \tag{19}$$

The linearized, continuous-time system in (18) is discretized at each sampling time $dt$ using Euler method. At each time instant $t = k$:

$$\begin{aligned}\frac{\mathbf{x}(k+1) - \mathbf{x}(k)}{dt} &= f(\mathbf{x}_o, u_o, \mathbf{w}_o) + \mathbf{A}(\mathbf{x}(k) - \mathbf{x}_o) \\ &\quad + \mathbf{B_u}(u(k) - u_o) + \mathbf{B_w}(\mathbf{w}(k) - \mathbf{w}_o) \\ \mathbf{x}(k+1) &= \mathbf{x}(k) + dt[f(\mathbf{x}_o, u_o, \mathbf{w}_o) + \mathbf{A}(\mathbf{x}(k) - \mathbf{x}_o) \\ &\quad + \mathbf{B_u}\Delta u(k) + \mathbf{B_w}(\mathbf{w}(k) - \mathbf{w}_o)] \\ \mathbf{x}(k+1) &= (\mathbf{I} + \mathbf{A}\cdot dt)\mathbf{x}(k) + \mathbf{B_u}\Delta u(k)\cdot dt \\ &\quad + \mathbf{B_w}(\mathbf{w}(k) - \mathbf{w}_o)dt + f(\mathbf{x}_o, u_o, \mathbf{w}_o)dt - \mathbf{A}\cdot\mathbf{x_o}\cdot dt\end{aligned} \tag{20}$$

The above model is used in the LMPC implementation to predict the oxygen storage system behavior over $N$ steps into the future. At the beginning of each prediction horizon, the system is linearized around a given nominal state $\mathbf{x_o}$ and input $u_o$, and $\mathbf{w_o}$. In (20), $\Delta u(k)$ represents the difference between the input at time $k$, $u(k)$, and the nominal input $u_o$.

The nominal state $\mathbf{x}_o$ needed for the linearization is obtained from an extended Kalman filter (EKF)[31] which estimates the oxygen storage level at the three spatial cells, for a given input $u_o$ and $\mathbf{w_o}$. It is noted that the nominal point for linearization may not be an equilibrium of the system. Therefore, the value of $f_0$ might not always be zero.

Overall, the discrete-time linearized system is given as:

$$\mathbf{x}(k+1) = \mathbf{A_d}\cdot\mathbf{x}(k) + \mathbf{B_d}\Delta u(k) + \mathbf{B}_\nu\nu \tag{21}$$

where

$$\begin{aligned}\mathbf{A_d} &= \mathbf{I} + \mathbf{A}\cdot dt \\ \mathbf{B_d} &= \mathbf{B_u}\cdot dt \\ \nu &= \mathbf{B_w}(\mathbf{w}(k) - \mathbf{w}_o)dt + f(\mathbf{x}_o, u_o, \mathbf{w}_o)dt - \mathbf{A}\cdot\mathbf{x_o}\cdot dt \\ \mathbf{B}_\nu &= \mathbf{I}\end{aligned}$$

and $\mathbf{A_d} \in \mathbb{R}^{\mathbf{3\times3}}$, $\mathbf{B_d} \in \mathbb{R}^{\mathbf{3\times1}}$, and $\mathbf{B}_\nu \in \mathbb{R}^{\mathbf{3\times3}}_{[\mathbf{0},\mathbf{1}]}$ were $\nu$ is a disturbance to the linearized system model with known values. The exhaust temperature and mass flow rate are generated from the engine model. The non-zero derivative terms (caused by linearizing the system at non-equilibrium) are computed directly using the nonlinear TWC dynamics model.

To assess the accuracy of the linearized model, used to predict the evolutiona of the system dynamics in place of the nonlinear one, a comparison with the nonlinear model response is carried out.

The linearized TWC oxygen storage model is reset to the nonlinear model response at the beginning of every prediction time horizon. Figure 6 shows a qualitative schematic of the behavior of the linearized model compared to the nonlinear one over a prediction horizon of lenght $N$. For the quantitative investigation, the nonlinear and linearized TWC oxygen storage model are simulated for four different sampling times $(0.005sec, 0.01sec, 0.05sec, 0.1sec)$ and three different lengths of prediction horizon ($N = 1$ time step, $N = 10$ time steps, $N = 20$ time steps). The performance of the nonlinear model and the linearized model are compared in terms of the average TWC oxygen storage level over the three descritized cells, $\bar{\phi}_i$, and normalized air-fuel ratio at the mid location, $\lambda_{mid}$. For each combination of sampling time and prediction horizon, the normalized RMSE for $\lambda_{mid}$ and $\bar{\phi}$ are computed as follows:

$$\begin{aligned}R_{\lambda_{mid}}(\%) &= \frac{100\times\sqrt{\frac{\sum_{t=1}^{K}(\lambda_{mid,nonlin,t} - \lambda_{mid,lin,t})^2}{K}}}{\lambda_{mid,nonlin,max} - \lambda_{mid,nonlin,min}} \\ R_{\bar{\phi}}(\%) &= \frac{100\times\sqrt{\frac{\sum_{k=1}^{K}(\bar{\phi}_{nonlin,k} - \bar{\phi}_{lin,k})^2}{K}}}{\bar{\phi}_{nonlin,max} - \bar{\phi}_{nonlin,min}}\end{aligned} \tag{22}$$

Here, the normalizations are done with respect to the range of $\lambda_{mid,nonlin}$ and $\bar{\phi}_{nonlin}$ from the nonlinear model, respectively. The fuel cutoff events are included in the computation in equation (22) since the identified model responds correctly to such events as shown in Figure 5.

In the catalyst, the exhaust mass flow rate and exhaust gas temperature change at every time step,

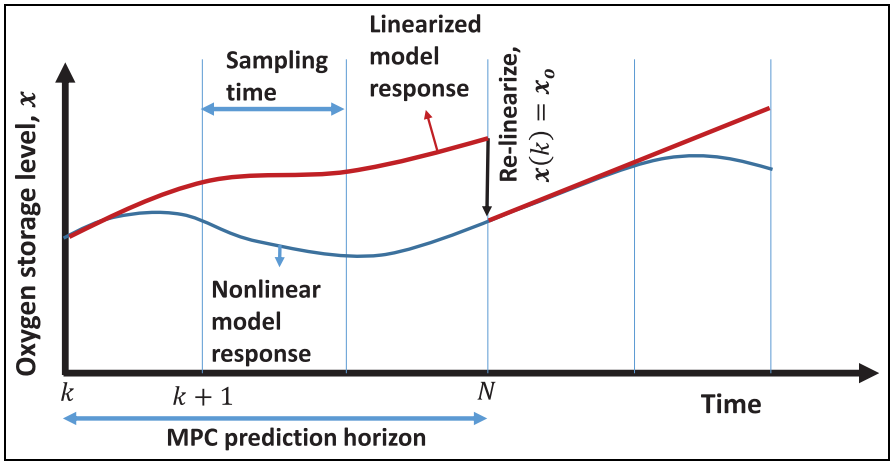


**Figure 6.** Graphical representation of nonlinear and linearized dynamics over the MPC prediction horizon.

**Table 2.** NRMSE of $\lambda_{mid}$ and $\bar{\phi}$ for a TWC aged to 150,000 miles over US06 cycle.

(a) Time varying linearized model.

| Time horizon steps ($N$) | 0.005 s | | 0.01 s | | 0.05 s | | 0.1 s | |
|---|---|---|---|---|---|---|---|---|
| | $NRMSE_{\bar{\phi}}$ (%) | $NRMSE_{\lambda_m}$ (%) | $NRMSE_{\bar{\phi}}$ (%) | $NRMSE_{\lambda_m}$ (%) | $NRMSE_{\bar{\phi}}$ (%) | $NRMSE_{\lambda_m}$ (%) | $NRMSE_{\bar{\phi}}$ (%) | $NRMSE_{\lambda_m}$ (%) |
| Simulation time step | | | | | | | | |
| 1 | 0 | 0 | 0 | 0 | 0 | 0 | 0 | 0 |
| 10 | 0.002 | 0.04 | 0.01 | 0.11 | 1.13 | 1.77 | 4.15 | 9.06 |
| 20 | 0.01 | 0.12 | 0.11 | 0.26 | 3.87 | 3.4 | 7.96 | 11.16 |

(b) Time invariant linearized model.

| Time horizon steps ($N$) | 0.005 s | | 0.01 s | | 0.05 s | | 0.1 s | |
|---|---|---|---|---|---|---|---|---|
| | $NRMSE_{\bar{\phi}}$ (%) | $NRMSE_{\lambda_m}$ (%) | $NRMSE_{\bar{\phi}}$ (%) | $NRMSE_{\lambda_m}$ (%) | $NRMSE_{\bar{\phi}}$ (%) | $NRMSE_{\lambda_m}$ (%) | $NRMSE_{\bar{\phi}}$ (%) | $NRMSE_{\lambda_m}$ (%) |
| Simulation time step | | | | | | | | |
| 1 | 0 | 0 | 0 | 0 | 0 | 0 | 0 | 0 |
| 10 | 0.002 | 0.04 | 0.01 | 0.11 | 1.88 | 1.62 | 3.62 | 6.16 |
| 20 | 0.01 | 0.13 | 0.11 | 0.26 | 4.28 | 3.45 | 7.65 | 8.04 |

causing the catalyst brick temperature to change. Since the brick temperature is a time varying parameter in the $\mathbf{A_d}$ matrix, to keep the linearized model time invariant, the exhaust gas temperature and exhaust mass flow rate are kept constant over the prediction horizon. Keeping the $\mathbf{A_d}$, $\mathbf{B_d}$, and $\nu$ matrices time invariant is important to reduce the complexity of the LMPC formulation. In reality, the exhaust gas temperature and mass flow rate change at every sampling time. Therefore, the assumption of constant $T_{exh}$ and $\dot{m}_{exh}$ within the prediction time horizon needs to be examined. For this purpose, two different cases are considered: (i) the $\mathbf{A_d}$, $\mathbf{B_d}$ matrices and the disturbance of the linearized model $\nu$ are time variant due to changes in $T_{exh}$ and $\dot{m}_{exh}$, (ii) the $\mathbf{A_d}$, $\mathbf{B_d}$ matrices and $\nu$ are time invariant. A comparison of these two cases is presented for simulation of the 150,000 miles aged catalyst model in Table 2 over the US06 drive cycle. The normalized RMS error between the nonlinear and linearized models are listed for different combinations of sampling time and prediction time horizon length, $N$. Results show that assuming time invariant values of the linearized model matrices does not impact the linearization accuracy significantly over these ranges of sampling time and prediction horizon. In fact, sometimes the accuracy is better for case (ii) compared to case (i) which can be attributed to the relative magnitude of $\lambda_{mid,\,lin}$ and $\bar{\phi}_{lin}$ compared to the magnitude of $\lambda_{mid,\,nonlin}$ and $\bar{\phi}_{nonlin}$, respectively. For larger sampling times, the discrepancy between the nonlinear and the linearized model increases. From the tables, a sampling time of 0.05 s and a prediction horizon of 10 time steps into the future, that is, $N = 10$, is selected for

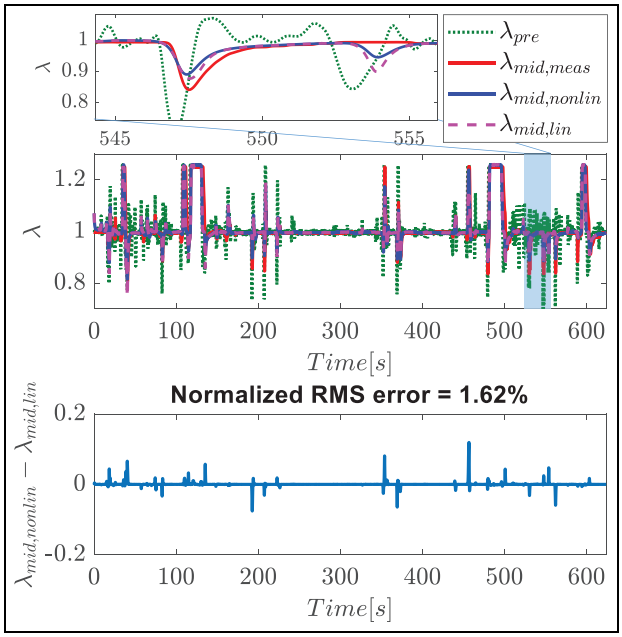


**Figure 7.** Comparison between the nonlinear and linearized model predictions of air-fuel ratio at the mid location with a sampling time of 0.05 s and prediction horizon containing 10 time steps in the future.

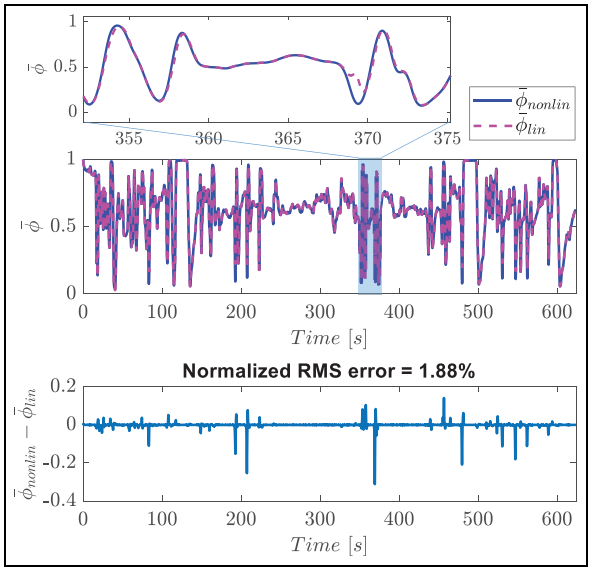


**Figure 8.** A comparison between the nonlinear and linearized model predictions of average oxygen storage level with sampling time of 0.05 s and prediction horizon containing 10 time steps in the future.

MPC implementation. Such a selection is based on the tradeoff between the accuracy of the linearized model and the computational load of the LMPC.

For accuracy comparison purposes, a specific case study is presented in Figures 7 and 8, where the 150,000 mile-aged catalyst model is simulated using US06 drive cycle with a sampling time of 0.05 s and a prediction time horizon of 10 time steps. The normalized air-fuel ratio at the mid location, $\lambda_{mid}$, and the average oxygen storage level, $\bar{\phi}$, are computed for both the nonlinear and linearized models and plotted against the experimental measurements as a baseline. The comparison for $\lambda_{mid}$ in Figure 7 shows that, for a sampling time of 0.05 s and prediction time horizon containing 10 time steps in the future, the normalized RMS error between the nonlinear and the linearized model is around 1.62%. Note that both models predict the usual TWC behavior where the $\lambda_{mid}$ response is damped and delayed compared to the $\lambda_{pre}$ signal. The error between the nonlinear and linearized models in terms of average oxygen storage level is shown in Figure 8. The figure shows acceptable agreement between the nonlinear and linearized oxygen storage level predictions with a normalized RMS error of only 1.88%.

## Linear model predictive control

For $N$ time steps into the future, the goal of MPC is to keep the oxygen storage level $\mathbf{x}(k)$ close to the reference $\bar{\mathbf{x}}_{ref}$ while minimizing the control effort (correction to the reference air-fuel ratio). Therefore, the overall optimization objective is to find the optimal air-fuel ratio correction $\mathbf{U}^*(k)$ over the prediction horizon of $N$ samples starting at time step $k$. The cost function to be minimized is given by:

$$J = [\sum_{i=0}^{N-1} (\mathbf{x}(k+i) - \bar{\mathbf{x}}_{ref}) \cdot \bar{\mathbf{Q}} \cdot (\mathbf{x}(k+i) - \bar{\mathbf{x}}_{ref})^T + p \cdot (u(k+i-1) - \bar{\lambda}(k+i-1))^2] \quad (23)$$

where, $i = 0, 1, ..., N-1$, $\bar{\mathbf{Q}} \in \mathbb{R}^{3\times3}_{>\mathbf{0}}, p \in \mathbb{R}_{>\mathbf{0}}$.

The nonlinear optimization problem can be formulated as follows:

$$\mathbf{U}^*(k) = \underset{\Delta u(k), ...\Delta u(k+N-1)}{\arg\min} J$$
subject to,
$$\mathbf{x}(k+1) = \mathbf{A_d} \cdot \mathbf{x}(k) + \mathbf{B_d}\Delta u(k) + \mathbf{B}_\nu \nu \quad (24)$$
$$\mathbf{x}_{min} \leqslant \mathbf{x}(k) \leqslant \mathbf{x}_{max}$$
$$\Delta u_{min} \leqslant \Delta u(k) \leqslant \Delta u_{max}$$

where $\mathbf{x}(k) = [\phi_1(k) \quad \phi_2(k) \quad \phi_3(k)]^T \in \mathbb{R}^{\mathbf{3}}_{[\mathbf{0},\mathbf{1}]}$ is the vector of estimated oxygen storage level in each cell from EKF at time step $k$, and $\mathbf{x}_{ref} = [\phi_{1,ref} \quad \phi_{2,ref} \quad \phi_{3,ref}]^T \in \mathbb{R}^{\mathbf{3}}_{[\mathbf{0},\mathbf{1}]}$ is the reference oxygen storage level vector.

In (24), $u(k) = \lambda_{pre}(k)$ and the operating point chosen for linearization at time step $k$ is $\bar{\lambda}(k) = u_o(k)$. Assuming that $\bar{\lambda}(k)$, dictated by the ECU, is constant over the prediction horizon, the normalized air-fuel ratio correction $\Delta u(k+i)$, at each sampling time $k+i$ is defined as follows:

$$\Delta u(k+i) = \lambda_{pre}(k+i) - \bar{\lambda}(k) \quad (25)$$

where, $i$ varies from 0 to $N-1$. In (24), $\bar{\mathbf{Q}}$ is a 3×3 diagonal matrix and $p$ is a scalar coefficent used to

change the relative weight of the two terms in the optimization objective.

To simplify the LMPC formulation, the disturbance term in (21) is discarded from the state dynamics and used to offset the state reference. Therefore, given the state $\mathbf{x}$ at time step $k$, the linearized state transitions into the future up to $N-1$ time steps, without the disturbance term, is defined as follows:

$$\begin{aligned}
\mathbf{x}(k+1|k) &= \mathbf{A_d}\cdot\mathbf{x}(k) + \mathbf{B_d}\Delta u(k)\\
\mathbf{x}(k+2|k) &= \mathbf{A_d}\cdot\mathbf{x}(k+1|k) + \mathbf{B_d}\Delta u(k+1)\\
&= \mathbf{A_d}^2\cdot\mathbf{x}(k) + \mathbf{A_d}\mathbf{B_d}\Delta u(k) + \mathbf{B_d}\Delta u(k+1)\\
&\dots\\
\mathbf{x}(k+N|k) &= \mathbf{A_d}^N\cdot\mathbf{x}(k) + \mathbf{A_d}^{N-1}\mathbf{B_d}\Delta u(k) + \dots\\
&\quad + \mathbf{B_d}\Delta u(k+N-1)
\end{aligned} \tag{26}$$

where, $\mathbf{x}(k+i|k)$ with $i=1,...,N$ represents the response of the linearized model at time step $k+i$ given the vector of state at time step $k$. Combining the state transition and input vector over the prediction horizon into a state vector, $\mathbf{X}(k)$, and input vector, $\mathbf{U}(k)$, the following expressions are obtained:

$$\begin{aligned}
\mathbf{X}(k) &= [\mathbf{x}(k+1|k) \quad \mathbf{x}(k+2|k)\dots\mathbf{x}(k+N|k)]^T\\
\mathbf{U}(k) &= [\Delta u(k) \quad \Delta u(k+1)\dots\Delta u(k+N-1)]^T
\end{aligned}$$

where,

$$\mathbf{X}(k)\in\mathbb{R}^{\mathbf{3N\times 1}}_{[\mathbf{0},\mathbf{1}]}, \quad \mathbf{U}(k)\in\mathbb{R}^{\mathbf{N}} \tag{27}$$

From (26) and (27), the discrete state transition at each sampling time within the prediction horizon, $\mathbf{X}(k)$, can be expressed as a function of the state at the beginning of the prediction horizon, $\mathbf{x}(k)$, and the input (normalized air-fuel ratio correction) at each sampling time, $\mathbf{U}(k)$. The combined linearized state dynamics over a prediction horizon is then defined as follows:

$$\mathbf{X}(k) = \mathbf{F}\cdot\mathbf{x}(k) + \mathbf{E}\cdot\mathbf{U}(k) \tag{28}$$

where $\mathbf{F}$ and $\mathbf{E}$ are matrices composed of the $\mathbf{A_d}$ and $\mathbf{B_d}$ matrices and defined as:

$$\begin{aligned}
\mathbf{F} &= [\mathbf{A_d} \quad \mathbf{A_d}^2 \quad \mathbf{A_d}^3\dots\mathbf{A_d}^N]^T\\
\mathbf{E} &= \begin{bmatrix}
\mathbf{B_d} & 0 & 0 & \dots & 0\\
\mathbf{A_d}\mathbf{B_d} & \mathbf{B_d} & 0 & \dots & 0\\
\mathbf{A_d}^2\mathbf{B_d} & \mathbf{A_d}\mathbf{B_d} & \mathbf{B_d} & \dots & 0\\
\vdots & \vdots & \vdots & \ddots & \vdots\\
\mathbf{A_d}^{N-1}\mathbf{B_d} & \mathbf{A_d}^{N-2}\mathbf{B_d} & \mathbf{A_d}^{N-3}\mathbf{B_d} & \dots & \mathbf{B_d}
\end{bmatrix}\\
&\text{where,} \quad \mathbf{F}\in\mathbb{R}^{\mathbf{3N\times 3}}, \quad \mathbf{E}\in\mathbb{R}^{\mathbf{3N\times N}}
\end{aligned} \tag{29}$$

The linearized model in (28) is derived upon linearization of the nonlinear model around an equilibrium point, $\mathbf{x_o}$, for which $\dot{\mathbf{x}}_o = f(\mathbf{x_o}, u_o) = 0$. However, in this work, the MPC linearizes the nonlinear TWC model at any state $\mathbf{x_o}$ and input $u_o$. This nominal condition may not be an equilibrium point of the system, therefore, $\dot{\mathbf{x}}_o = f(\mathbf{x_o}, u_o)$ may not be equal to zero. The nonzero nominal value of the system is incorporated into the state-space model through vector $\mathbf{V}$ as follows:

$$\mathbf{X}_\nu(k) = \mathbf{F}\cdot\mathbf{x}(k) + \mathbf{E}\cdot\mathbf{U}(k) + \mathbf{E}_\nu\cdot\mathbf{V} \tag{30}$$

where, $\mathbf{V}$ is a column vector of disturbances for $N$ samples ($\mathbf{V} = [\nu\dots\nu]^T\in\mathbb{R}^{\mathbf{N}}$) and $\mathbf{E}_\nu\in\mathbb{R}^{\mathbf{3N\times N}}$ is generated similar to $\mathbf{E}$ by replacing $\mathbf{B_d}$ with $\mathbf{B}_\nu$. Since the disturbance is constant over the prediction horizon, the linearized state dynamics in (28) can be used in the MPC framework if the reference at each sampling time is offset by the amount of the disturbance. Over the prediction horizon, the reference oxygen storage level is defined by $\bar{\mathbf{X}}_{ref}$ as follows:

$$\bar{\mathbf{X}}_{ref} = [\bar{\mathbf{x}}_{ref} \quad \bar{\mathbf{x}}_{ref}\dots\bar{\mathbf{x}}_{ref}]^T\in\mathbb{R}^{\mathbf{3N\times 1}}_{[\mathbf{0},\mathbf{1}]} \tag{31}$$

Offsetting the reference by the disturbance vector, the following state reference is obtained:

$$\bar{\mathbf{X}}_{ref,\nu} = \bar{\mathbf{X}}_{ref} - \mathbf{E}_\nu\cdot\mathbf{V} \tag{32}$$

where, $\bar{\mathbf{X}}_{ref,\nu}\in\mathbb{R}^{\mathbf{3N\times 1}}$. With the above simplifications, the original nonlinear optimization problem in (24) is transformed into a quadratic programming (QP) problem, as shown in (33). The QP problem is solved at each sampling time $k$ to obtain the optimal control sequence $\mathbf{U}^*(k)$ over the prediction horizon, as

$$\begin{aligned}
&\mathbf{U}^*(k) = \underset{\Delta u(k),\dots\Delta u(k+N-1)}{\arg\min}\\
&([\mathbf{X}(k) - \bar{\mathbf{X}}_{ref,\nu}]\cdot\tilde{\mathbf{Q}}\cdot[\mathbf{X}(k) - \bar{\mathbf{X}}_{ref,\nu}]^T\\
&\quad + \mathbf{U}^T(k)\cdot\mathbf{P}\cdot\mathbf{U}(k)))\\
&\text{subject to,}\\
&\quad \mathbf{X}(k) = \mathbf{F}\cdot\mathbf{x}(k) + \mathbf{E}\cdot\mathbf{U}(k)\\
&\quad \mathbf{X}_{min}\leqslant\mathbf{X}(k)\leqslant\mathbf{X}_{max}\\
&\quad \mathbf{U}_{min}\leqslant\mathbf{U}(k)\leqslant\mathbf{U}_{max}
\end{aligned} \tag{33}$$

where

$$\tilde{\mathbf{Q}} = \begin{bmatrix}
\bar{\mathbf{Q}} & \dots & \mathbf{0}\\
\vdots & \ddots & \mathbf{0}\\
\mathbf{0} & \mathbf{0} & \bar{\mathbf{Q}}
\end{bmatrix}\in\mathbb{R}^{\mathbf{3N\times 3N}}_{>\mathbf{0}}$$

$$\mathbf{P} = \begin{bmatrix}
p & \dots & 0\\
\vdots & \ddots & 0\\
0 & 0 & p
\end{bmatrix}\in\mathbb{R}^{\mathbf{N\times N}}_{>\mathbf{0}}$$

where, for the problem solved in this paper, $\mathbf{X}_{min} = 0$, $\mathbf{X}_{max} = 1$, $\mathbf{U}_{min} = -0.2$, and $\mathbf{U}_{max} = 0.2$.

## Implementation of linear MPC

The goal of LMPC is to regulate oxygen storage levels in three discrete TWC cells to thier respective reference values by controlling the air-fuel ratio command given

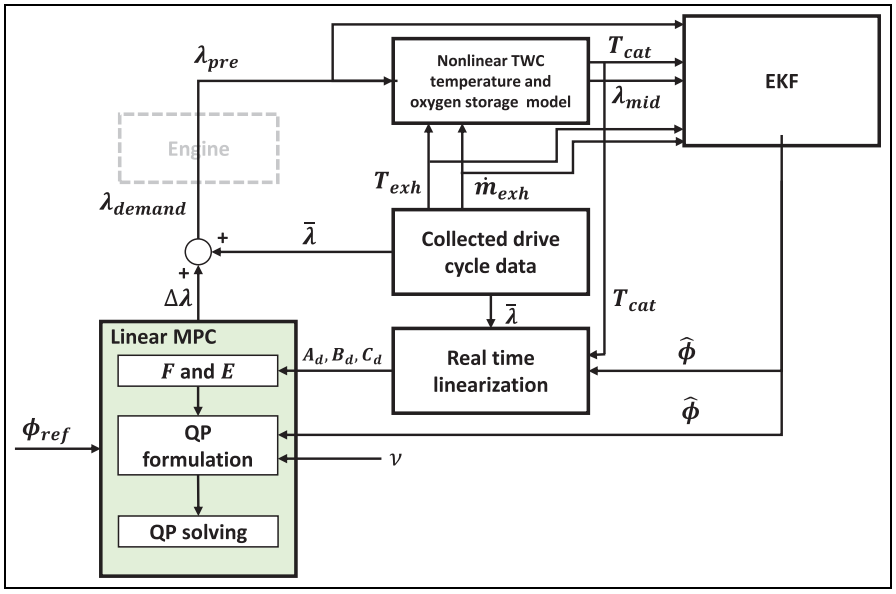


**Figure 9.** Block diagram for offline simulation of linear MPC for tracking a reference oxygen storage level in TWC. Since engine dynamics are not modeled in the offline simulation, the demanded specific air-fuel ratio from LMPC, $\lambda_{demand}$ is assumed to be the same as the pre catalyst specific air-fuel ratio, $\lambda_{pre}$.

to the engine. The LMPC utilizes the state estimate from EKF, developed in Gelmini et al.[31] which takes into account the uncertainties in model accuracy and sensor measurements. The EKF has the ability to estimate both the dynamic oxygen storage level and the oxygen storage capacity (OSC).[32] In this work, it is assumed that the OSC is constant during the testing duration for the given catalyst. The constant OSC is preemptively identified using the identification procedure outlined in Section 3.

In this paper, an offline simulation framework is developed to investigate the tracking performance of LMPC. Figure 9 presents a block diagram of the offline LMPC simulation utilizing the exhaust gas temperature $T_{exh}$, and mass flow rate $\dot{m}_{exh}$, obtained during vehicle operation over a US06 drive cycle, shown in Figure 4.

These inputs are used to estimate the oxygen storage levels, $\hat{\phi}$, calculate brick temperature, $T_{cat}$, and normalized air-fuel ratio at the mid location, $\lambda_{mid}$. These quantities, along with the desired normalized air-fuel ratio obtained from the ECU, $\bar{\lambda}$, are used for real-time linearization of the nonlinear TWC oxygen storage dynamics. The linearized TWC model is used to solve the QP problem defined in (33) to find the normalized air-fuel ratio correction, $\Delta\lambda(k)$, such that the desired normalized air-fuel ratio signal generated by the vehicle ECU is a constant value of stoichiometry, that is, $\bar{\lambda} = 1$. In the offline simulation, the same desired air-fuel ratio is used upon which MPC makes the correction to track the reference oxygen storage level. The reference oxygen storage level vector, $\phi_{\mathbf{ref}}$, and the disturbance vector, $\nu$, from (21) are used in the LMPC framework to calculate $\bar{\mathbf{X}}_{ref,\nu}$ from (32). Engine dynamics are not considered in the LMPC formulation of this study. Therefore, the pre-catalyst normalized air-fuel ratio can be expressed as a sum of the desired air-fuel ratio and the correction made by MPC, such that, $\lambda_{pre}(k) = \bar{\lambda}(k) + \Delta\lambda(k)$.

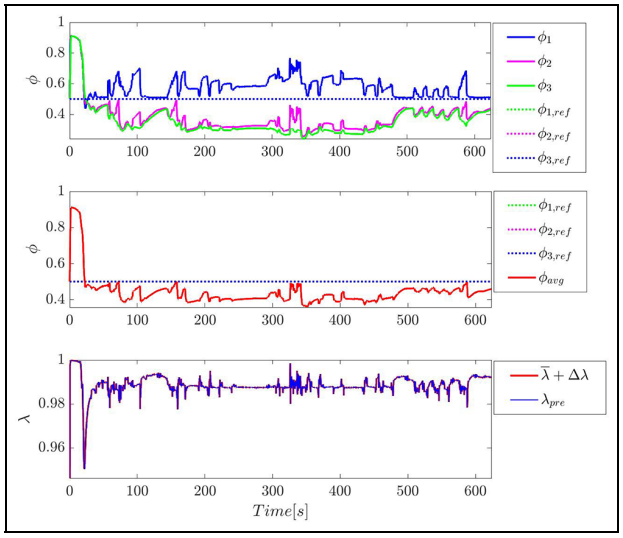


**Figure 10.** Offline performance of the linear MPC oxygen storage level tracking with $\phi_{\mathbf{ref}} = [0.5 \quad 0.5 \quad 0.5]$ using US06 drive cycle data.

Figure 10 shows the simulation results for LMPC implementation where the goal is to track a spatially discretized reference oxygen storage level vector, $\phi_{\mathbf{ref}} = [0.5 \quad 0.5 \quad 0.5]$. A bound on $\Delta\lambda$ is imposed $(-0.2 \leqslant \Delta\lambda \leqslant 0.2)$ in accordance with the physical system's ability to respond to a given command. In the top plot of Figure 10, the oxygen storage level at cell 1 is higher than the other two cells. Cell 1 is closest to the inlet, therefore, it responds quickly to any change in the air-fuel ratio command compared to other cells. Since the oxygen storage level of the cells are dependent

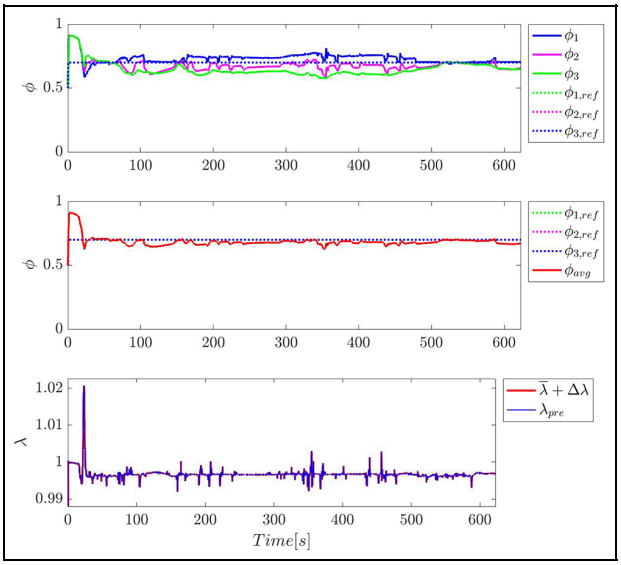


**Figure 11.** Offline performance of the linear MPC oxygen storage level tracking with $\phi_{\mathbf{ref}}$ = [0.7 0.7 0.7] using US06 drive cycle data.

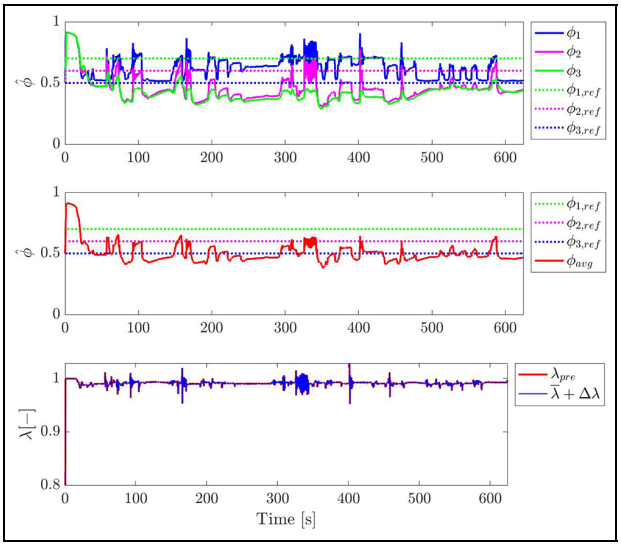


**Figure 12.** Offline performance of the linear MPC oxygen storage level tracking with $\phi_{\mathbf{ref}}$ = [0.7 0.6 0.5] using US06 drive cycle data[AQ: 1].

on one another, it is not possible to achieve the same tracking performance for each cell by controlling the input air-fuel ratio correction command, $\Delta\lambda(k)$. As a result, the oxygen storage level of cell 2 and cell 3 remains below the reference setpoint and overall, the average oxygen storage level is close to the desired reference. Note that, the experimentally validated TWC model assumes an oxygen concentration of 1% at the stoichiometric value of $\lambda_{pre}$. Therefore, to maintain a constant oxygen storage level, the corrected pre-catalyst normalized air-fuel ratio signal, $\lambda_{pre}$ operates just below the stoichiometric value of 1. Figure 11 shows similar tracking performance when the reference

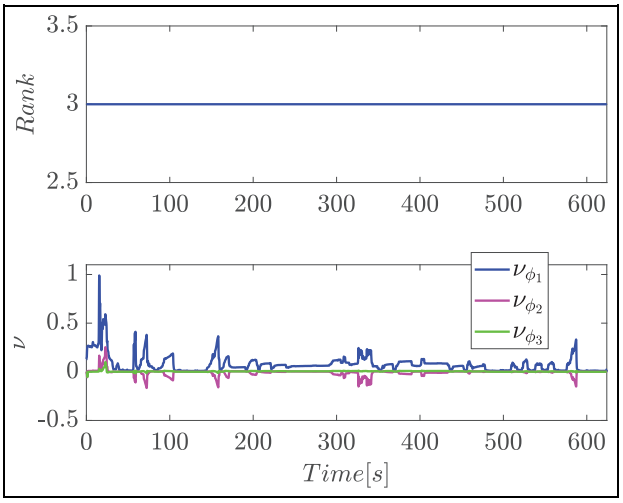


**Figure 13.** Rank of the controllability matrix of the linearized TWC model (top), and the disturbance term, $\nu$ from equation (21) (bottom).

is changed to $\phi_{\mathbf{ref}}$ = [0.7 0.7 0.7]. In both cases, the initial tracking error can be attributed to the uncertainty of the initial state estimation given to the EKF. Figure 18 shows the controller tracking capability to a reference $\phi_{\mathbf{ref}}$ = [0.7 0.6 0.5].

Since the LMPC is required to track the oxygen storage levels of three discrete blocks by controlling only the air-fuel ratio command, it is necessary to understand the controllability of the linearized system. Controllability is the ability to transfer the system state from an initial condition to any final state in a finite time. The controllability of the linearized TWC system is assessed by generating a controllability matrix of the discrete linearized system given in (21) and calculating the rank of the controllability matrix at every sampling time. Figure 13 shows that the rank of the controllability matrix is 3 at each time instant while tracking $\phi_{\mathbf{ref}}$ = [0.5 0.5 0.5] over the US06 drive cycle. Figure 13 also shows that the time varying disturbance, $\nu$, is significant at the inlet and diminishes along the length of the TWC. Therefore, the oxygen storage level at the inlet is more sensitive to the disturbance inputs, that is, mass flow rate and exhaust temperature than the oxygen storage level at downstream of the TWC.

In Figure 14, the simulated normalized air-fuel ratio at the mid TWC location utilizing the LMPC controller, $\lambda_{mid,mpc}$ is compared with the measured normalized air-fuel ratio at the mid TWC location, $\lambda_{mid,meas}$ (from Figure 7). For the purpose of comparison, the emission control strategy installed in the vehicle by the vehicle manufacturer is denoted as the "baseline strategy" and the quantity $\lambda_{mid,meas}$ is used here to evaluate the control performance of the "baseline strategy." The simulated $\lambda_{mid,mpc}$ has fewer and less severe excursions compared to $\lambda_{mid,meas}$. The average oxygen storage level estimated for the experimental data, $\phi_{avg,baseline}$ are then compared with the average oxygen storage level, $\phi_{avg,mpc}$ obtained after linear MPC implementation for

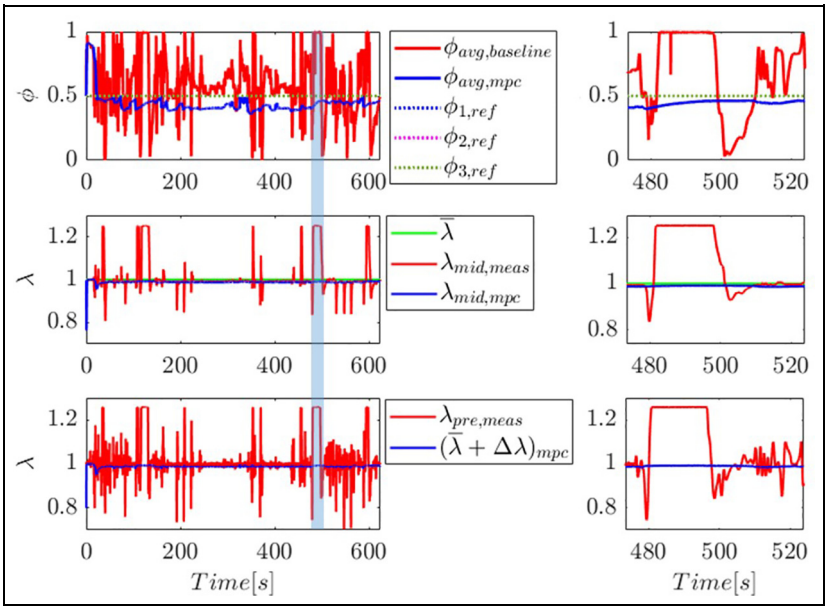


**Figure 14.** Comparison between the offline linear MPC, tracking $\phi_{\mathbf{ref}}$ = [0.5 0.5 0.5], and the baseline strategy in terms of $\phi_{avg}$ and $\lambda_{mid}$ using US06 drive cycle data when $\bar{\lambda}$ in MPC is a constant of 1.

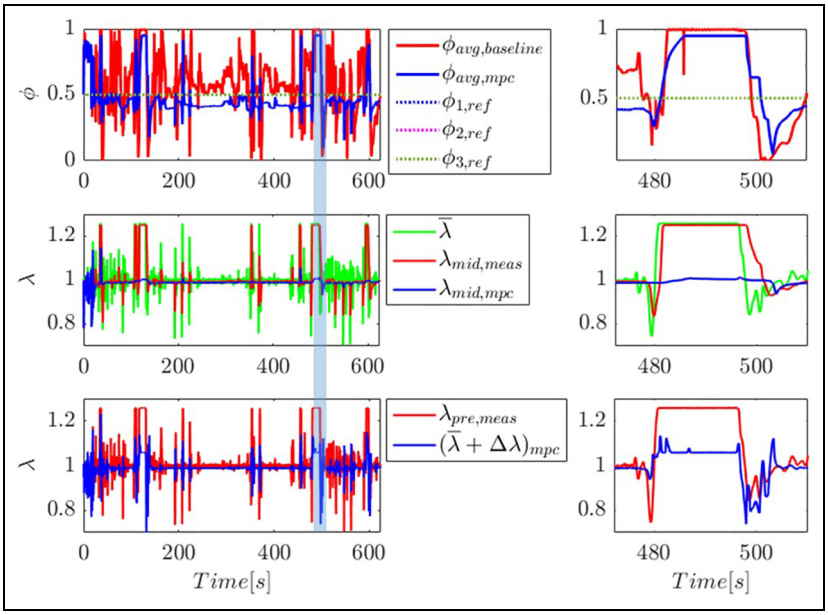


**Figure 15.** Comparison between the offline linear MPC, tracking $\phi_{\mathbf{ref}}$ = [0.5 0.5 0.5], and the baseline strategy in terms of $\phi_{avg}$ and $\lambda_{mid}$ using US06 drive cycle data when $\bar{\lambda}$ in MPC is the same as the $\lambda_{pre}$ from the baseline.

tracking $\phi_{\mathbf{ref}}$ = [0.5 0.5 0.5]. The estimated average oxygen storage level from LMPC is steadier than the baseline oxygen storage level estimated and confirms the effectiveness of the proposed LMPC approach for improved emission control.

Another comparison is made between the offline LMPC controller and stock ECU air-fuel ratio controller, where the pre-TWC air-fuel ratio, $\lambda_{pre}$, measured during the US06 drive cycle test (Figure 4) is assumed as $\bar{\lambda}$ in the LMPC controller. In that case, $\Delta\lambda$ corrections are made by the LMPC at each time step to track the desired oxygen storage level, such that, the commanded normalized air-fuel ratio becomes, $\lambda_{pre,mpc}(t) = \lambda_{pre,meas}(t) + \Delta\lambda(t)$. The comparison in Figure 15 shows that the LMPC implementation still results in fewer fluctuations of average oxygen storage level and smaller excursions of $\lambda_{mid}$ compared to the baseline vehicle controller. Thus, implementation of LMPC of TWC oxygen storage level presents an opportunity for the automotive industry to develop a TWC design that is smaller in size, saving capital cost.

The developed LMPC algorithm is also fast enough for real time control. As outlined in the next section, the LMPC controller is implemented and

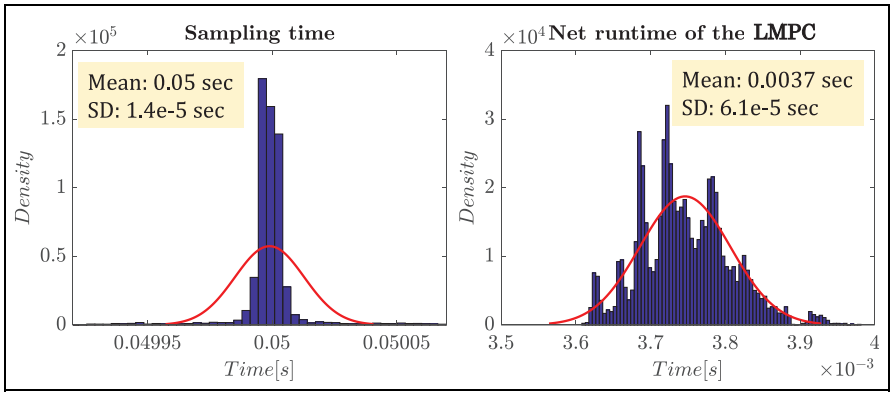


**Figure 16.** Distribution of sampling time of the ETAS system (left), and distribution of the execution time of LMPC (right).

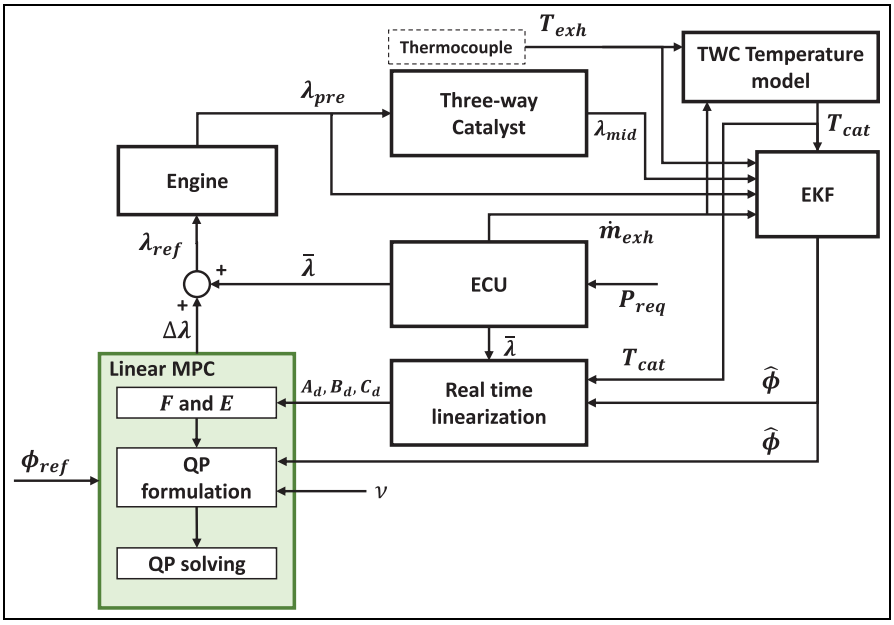


**Figure 17.** Block diagram for real-time tracking of reference oxygen storage level in a TWC using linear MPC.

communicated to the vehicle ECU using an ETAS INCA software platform. The time that the ETAS system takes to execute the LMPC code, can be a limiting factor for LMPC implementaiton in real time. A computational time analysis of ETAS system in Figure 16 shows that the execution time of the developed LMPC algorithm is about 3.8 ms which is much smaller than the system sampling time of 50 ms. Here, the sampling time is the time used to discretize the MPC strategy as given in Table 2.

Additionally, the efficient, low calibration effort of the LMPC emission control algorithm can significantly reduce the total aftertreatment system development cost. Figure 15 also shows that excessive richness of the commanded air-fuel ratio mixture can be avoided through implementation of the proposed LMPC control design, which exhibits smaller rewetting enrichment drops in $\lambda_{pre,meas}$ after fuel cutoff events. Reducing these rich air-fuel ratio excursions has the potential to improve the vehicle fuel economy during real world operation.

## Future work

Online implementation of the proposed LMPC in a vehicle is a topic of future research by the authors. Figure 17 shows a block diagram explaining how LMPC will be implemented in a vehicle to track reference oxygen storage levels at different longitudinal locations within the TWC. First, the exhaust gas temperature, $T_{exh}$, obtained from a thermocouple and $\dot{m}_{exh}$ obtained from the ECU will be used in the TWC temperature model to calculate the brick temperature, $T_{cat}$. Based on the measured and calculated signals: $T_{exh}$, $T_{cat}$, $\dot{m}_{exh}$, $\lambda_{pre}$, and $\lambda_{mid}$, the TWC oxygen storage levels will be estimated from the EKF. The desired normalized air-fuel ratio signal, $\bar{\lambda}$ in the ECU will be modified by the LMPC based on the difference between estimated state $\hat{\phi}$ and reference state $\phi_{ref}$. The corrected air-fuel ratio command, $\lambda_{ref}$ will be given to the engine. After the air-fuel ratio command is executed in the engine, the pre-catalyst normalized air fuel ratio, $\lambda_{pre}$

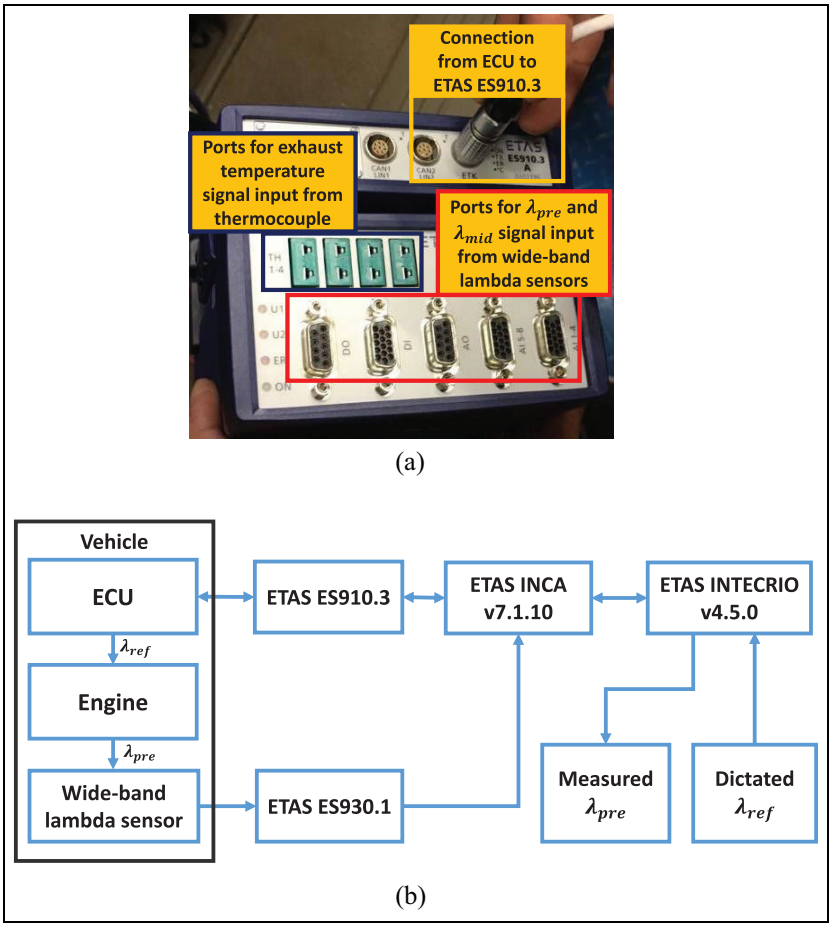


**Figure 18.** (a) Communication boxes to obtain signals from the ECU and sensors and (b) information flow diagram for engine delay characterization test in the vehicle.

will be measured and the entire procedure will be repeated at the next time step.

The modern gasoline engine is a complex dynamic system where the speed and magnitude of the response depend on numerous mechanical, thermal, and chemical factors. In the air-fuel ratio control literature, engine dynamics are often captured using empirical response models,[18,33] of the intake manifold, fueling, combustion, and crankshaft dynamics,[34] or neural network-based models.[10] The real-time implementation of the developed LMPC algorithm requires a reasonably accurate engine model. Modeling the engine dynamics and including an engine model within the LMPC framework to capture the dynamic delay behavior is the subject of ongoing research. However, it is important to understand delay's dependence on factors such as, engine RPM, load, frequency of the input signal, etc. In this paper, the following tests are performed to understand the type and time scale of the delay:

- A step $\lambda_{ref}$ is dictated to the engine and $\lambda_{pre}$ upstream of the catalyst is measured.
- A sinosoidal $\lambda_{ref}$ signal is dictated at different speeds and loads, and $\lambda_{pre}$ upstream of the catalyst is measured.
- A sinosoidal $\lambda_{ref}$ signal with varying frequency is dictated and $\lambda_{pre}$ upstream of the catalyst is measured.

The above tests are performed in the same vehicle in which the drive cycle data are obtained for TWC model parameter identification in Section 2. Communication to the vehicle ECU is established through ETAS INCA (v7.1.10) software. The ECU parameters are transferred to INCA via an ETAS ES910.3 communication unit and measurements from the wide-band lambda sensor are transferred via ETAS ES930.1 supplemental communication unit. The test profiles are converted from MATLAB/Simulink environment to the INTECRIO Real-time Target (IRT) format. The IRT build file is then compiled in ETAS INTECRIO (v4.5.0) software to communicate with the ECU via the INCA platform. Figure 18(a) shows the ports of the communication boxes to connect to the ECU and the sensors, and Figure 18(b) presents an information flow diagram for engine delay testing.

It is known from the literature that there are multiple factors contributing to the engine delay.[20] In order to understand the dynamics between $\lambda_{ref}$ (input) and $\lambda_{pre}$ (output), step tests were carried out experimentally, and

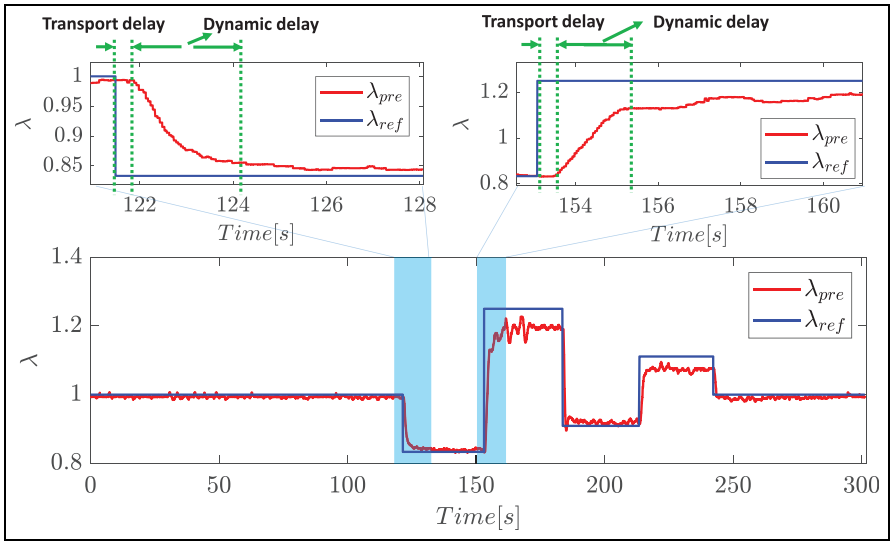


**Figure 19.** Engine response in terms of $\lambda_{pre}$ due to a step $\lambda_{ref}$ command given to the engine.

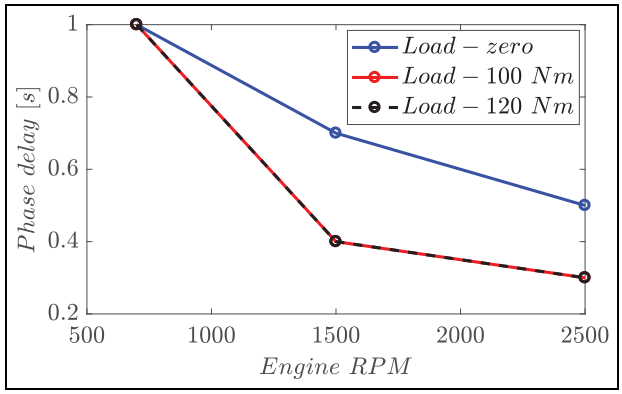


**Figure 20.** Phase delay between commanded $\lambda_{ref}$ and measured $\lambda_{pre}$ when a sinosoidal $\lambda_{ref}$ with constant frequency and amplitude is given to the engine as input.

presented in Figure 19. A transport delay at the beginning of a step change and a subsequent dynamic delay are observed. The step change command also shows a higher magnitude reduction in the lean region than the rich region.

To understand these effects, a sinusoidal $\lambda_{ref}$ signal with constant amplitude (0.2) and frequency (1 Hz) is applied when the engine RPM is kept constant around 700, 1500, and 2500 RPM. The vehicle load is then altered while keeping the RPM constant by running the chassis-dyno in the speed mode. Results in Figure 20 show that the delay changes with the engine RPM. The delay does not change significantly with load but changes from "no load" condition to "loaded" condition. The engine transients are faster at higher RPM and torque, therefore, the engine responds quickly to the given fueling signal resulting a shorter delay.

To understand how the engine responds to different frequency A/F commands, a sinosoidal $\lambda_{ref}$ command (Figure 21) with frequency varying from 0.001 to 20 Hz

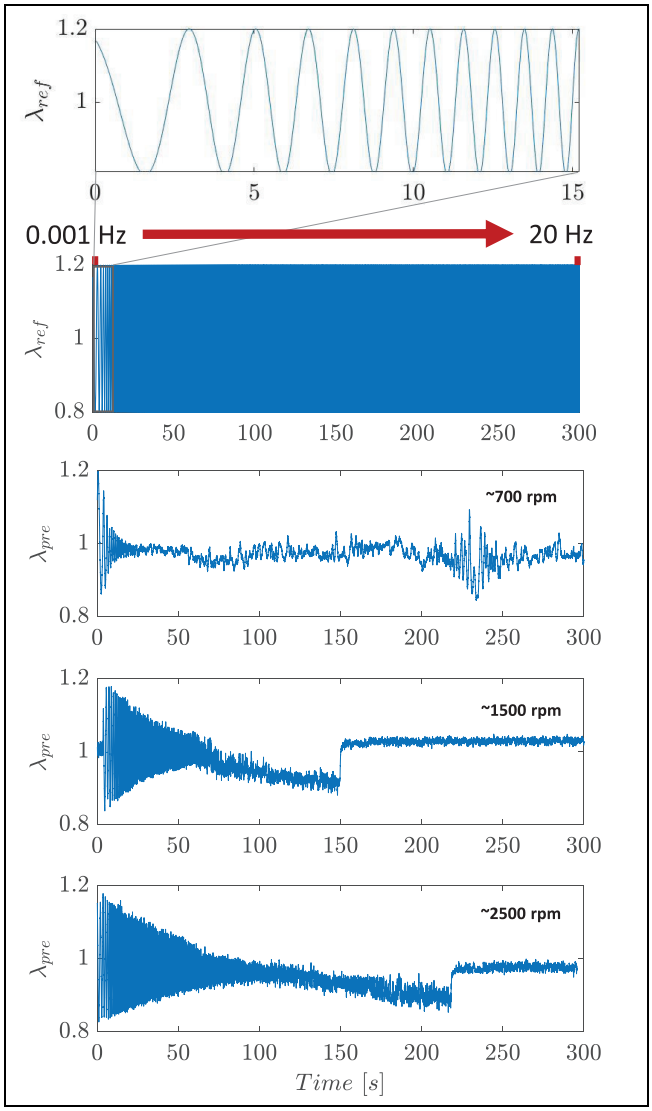


**Figure 21.** Phase delay between commanded $\lambda_{ref}$ and measured $\lambda_{pre}$ when a sinosoidal $\lambda_{ref}$ with constant frequency and amplitude is given to the engine as input.

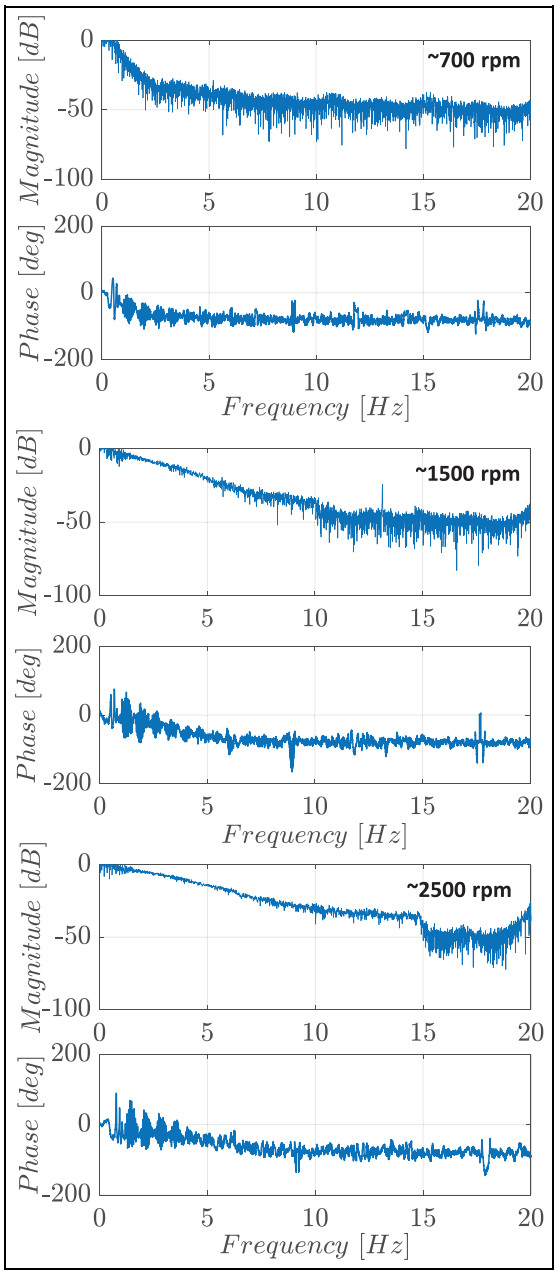


**Figure 22.** Phase delay between commanded $\lambda_{ref}$ and measured $\lambda_{pre}$ when a sinosoidal $\lambda_{ref}$ with varying frequency and constant amplitude is given to the engine as an input.

with a fixed amplitude is applied while running the engine in neutral, at 1500 RPM, and 2500 RPM with zero load. The measured $\lambda_{pre}$ response in Figure 21 shows significant amplitude decay with increased frequency. A shift toward the lean region is also visible in the $\lambda_{pre}$ response. After around 10 Hz at 1500 RPM, and around 15 Hz at 2500 RPM, the engine stops responding to the $\lambda_{ref}$ command. This might be the result of anti-noise safety features programmed within the vehicle.

To better understand the frequency and phase shift, the time domain input and output signals are converted into the frequency domain by fast fourier transformation (FFT). The difference in magnitude and phase of the commanded $\lambda_{ref}$ FFT and the measured $\lambda_{pre}$ FFT are presented in Figure 22. From the top plot, it is clear that at ~700 RPM, the amplitude of the sine wave drops by an order of magnitude (−20 dB) at approximately 1.5 Hz. The phase lag also reaches around 70° at 1.5 Hz. Since the MPC updates information at a frequency of 20 Hz (0.05 s), the relatively slow engine dynamics must be included in the MPC for it to accurately predict the future response. At higher engine speeds, the magnitude and phase plot exhibit a similar behavior. However, due to the faster engine dynamics, the magnitude decay occurs at a higher frequency (approximately 5 Hz for 1500 RPM, and 6.5 Hz for 2500 RPM). Thus, without the inclusion of an engine model in the LMPC, the LMPC needs to operate on a time scale of 1.5 Hz, that is, a sampling time of 0.6 s, to prevent the lambda response magnitude reduction from failing more than an order of magnitude for engine speeds greater than 700 RPM. Such a large sampling time will induce substantial error in the linearized model response. Therefore, inclusion of a suitable engine model is essential for the LMPC to work in real-time.

An RPM dependent delay model, engine map-based empirical model, and physics-based model are choices under consideration for future implementation.

## Conclusion

This paper develops a linear model predictive control framework using a linearized, physics-based TWC model to track a desired oxygen storage level in the catalyst. A nonlinear TWC temperature and oxygen storage model is identified through optimization using a PSO. The identified nonlinear oxygen storage model is linearized, and the accuracy of the linearized model has reasonable accuracy over a range of sampling times and prediction time horizons. Using the linearized model, an LMPC framework is developed to track a reference oxygen storage level in the TWC by controlling the normalized air-fuel ratio command. Simulation results confirm that the LMPC can successfully track desired oxygen storage levels at different longitudinal locations in a TWC. The proposed framework can also allows track a time varying trajectory of desired oxygen storage levels. This capability provides greater flexibility in controlling harmful emissions that depend on the TWC oxygen content.

The proposed controller shows less excursions of post-catalyst air fuel ratio and steadier oxygen storage levels than the baseline vehicle controller. Potential fuel economy benefits could be inferred from an air-fuel ratio command with fewer and less severe excursions in the rich region, especially after fuel cutoff events.

Successful implementation of the proposed LMPC framework in real-time is constrained by the engine delay dynamics. The delay dynamics shows dependence on RPM, load, and frequency variation of the

commanded normalized air-fuel ratio signal. The delay analysis herein provides confidence that the proposed LMPC framework can be successfully implemented in real-time if engine delay dynamics are configured within the MPC design either empirically or through an engine model.

## Acknowledgements

The authors greatly acknowledge the financial support from FCA US LLC (Auburn Hills, MI 48326, USA), under which this work was conducted. The authors are also grateful to Sean Moser, Dhruvang Rathod, and Rohit Koli from Clemson University International Center for Automotive Research (CU-ICAR) for their help and support during in-vehicle testing.

## Declaration of conflicting interests

The author(s) declared no potential conflicts of interest with respect to the research, authorship, and/or publication of this article.

## Funding

The author(s) disclosed receipt of the following financial support for the research, authorship, and/or publication of this article: The financial support of National Science Foundation through the CAREER Award Number CMMI-1839050 is acknowledged.

## ORCID iDs

Abdullah-al Mamun https://orcid.org/0000-0001-9462-6378
Simona Onori https://orcid.org/0000-0002-6556-2608

## References

1. Heinrich J, Schwarze PE, Stilianakis N, et al. Studies on health effects of transport-related air pollution. In: *Health effects of transport-related air pollution*, 2005, p.125. [AQ: 2]
2. Yim SH and Barrett SR. Public health impacts of combustion emissions in the United Kingdom. *Environ Sci Technol* 2012; 46(8): 4291–4296.
3. EPA emission standards regulations, https://www.epa.gov/emission-standards-reference-guide/epa-emission-standards-regulations (2017). [AQ: 3]
4. Young LC and Finlayson BA. *Mathematical modeling of the monolith converter*. ACS Publications, 1974. [AQ: 4]
5. Canale RP, Winegarden SR, Carlson CR, et al. General motors phase II catalyst system. *SAE technical paper, technical report*, 1978.
6. Tomforde M, Drewelow W, Duenow P, et al. A post-catalyst control strategy based on oxygen storage dynamics. *SAE technical paper, technical report*, 2013.
7. Ebrahimi B, Tafreshi R, Masudi H, et al. A parameter-varying filtered PID strategy for air–fuel ratio control of spark ignition engines. *Control Eng Pract* 2012; 20(8): 805–815.
8. Okazaki S, Kato N, Kako J, et al. Development of a new model based air-fuel ratio control system. *SAE Int J Engines* 2009; 2(1): 335–343.
9. Grizzle JW, Dobbins KL and Cook JA. Individual cylinder air-fuel ratio control with a single ego sensor. *IEEE Trans Veh Technol* 1991; 40(1): 280–286.
10. Wong PK, Wong HC, Vong CM, et al. Model predictive engine air-ratio control using online sequential extreme learning machine. *Neural Comput Appl* 2016; 27(1): 79–92.
11. Zhai Y-J, Yu D-W, Guo H-Y, et al. Robust air/fuel ratio control with adaptive DRNN model and AD tuning. *Eng Appl Artif Intell* 2010; 23(2): 283–289.
12. Auckenthaler TS. *Modelling and control of three-way catalytic converters*. ETH Zurich, 2005. [AQ: 5]
13. Choi SB and Hedrick JK. An observer-based controller design method for improving air/fuel characteristics of spark ignition engines. *IEEE Trans Control Syst Technol* 1998; 6(3): 325–334.
14. Balenovic M and Backx T. Model-based predictive control of a three-way catalytic converter. In: *Proceedings of the 2001 IEEE international conference on control applications (CCA'01)*, 2001, pp.626–631. New York: IEEE. [AQ: 6]
15. Balenovic M, Backx T and de Bie T. Development of a model-based controller for a three-way catalytic converter. *SAE technical paper, technical report*, 2002.
16. Muske KR and Jones JCP. Multi-objective model-based control for an automotive catalyst. *J Process Control* 2006; 16(1): 27–35.
17. Mallik A. State feedback based control of air-fuel-ratio using two wide-band oxygen sensors. In: *2015 10th Asian control conference (ASCC)*, 2015, pp.1–6. New York: IEEE. [AQ: 7]
18. Trimboli S, Di Cairano S, Bemporad A, et al. Model predictive control for automotive time-delay processes: an application to air-to-fuel ratio control. *IFAC Proc Vol* 2009; 42(14): 90–95.
19. Brandt EP, Wang Y and Grizzle JW. A simplified three-way catalyst model for use in on-board SI engine control and diagnostics. In: *Proceedings of the ASME dynamic system and control division*, 1997, vol. 61, pp.653–659. [AQ: 8]
20. Guzzella L and Onder C. *Introduction to modeling and control of internal combustion engine systems*. Springer Science & Business Media, 2009. [AQ: 9]
21. Rawlings J and Mayne D. *Model predictive control: theory and design (Nob Hill Pub)*, 2009. [AQ: 10]
22. Ferreau HJ, Kirches C, Potschka A, et al. qpOASES: a parametric active-set algorithm for quadratic programming. *Math Progr Comput* 2014; 6(4): 327–363.
23. Wright SJ. *Primal-dual interior-point methods*. Philadelphia: SIAM, 1997.
24. Bemporad A. Model predictive control design: new trends and tools. In: *2006 45th IEEE conference on decision and control*, 2006, pp.6678–6683. New York: IEEE. [AQ: 11]
25. Bemporad A. Model predictive control of turbocharged gasoline engines for mass production. *SAE technical paper 2018-01-0875*, 2018.
26. Sabatini S, Gelmini S, Hoffman MA, et al. Design and experimental validation of a physics-based oxygen storage—thermal model for three way catalyst including aging. *Control Eng Pract* 2017; 68: 89–101.
27. Kiwitz P, Onder C and Guzzella L. Control-oriented modeling of a three-way catalytic converter with

observation of the relative oxygen level profile. *J Process Control* 2012; 22(6): 984–994.
28. Herz RK. Dynamic behavior of automotive catalysts. 1. Catalyst oxidation and reduction. *Ind Eng Chem Prod Res Dev* 1981; 20(3): 451–457.
29. Sabatini S, Kil I, Dekar J, et al. A new semi-empirical temperature model for the three way catalytic converter. In: *2015 IFAC workshop on engine and powertrain control, simulation and modeling*, 2015. [AQ: 12]
30. Kang SB, Han SJ, Nam I-S, et al. Detailed reaction kinetics for double-layered Pd/Rh bimetallic TWC monolith catalyst. *Chem Eng J* 2014; 241: 273–287.
31. Gelmini S, Sabatini S, Hoffman MA, et al. Development and experimental validation of a dual extended Kalman filter for three way catalytic converter. In: *American control conference*, 2017, pp.5386–5391. New York: IEEE.[AQ: 13]
32. Sabatini S, Kil I, Dekar J, et al. Characterization of aging effect on three way catalyst oxygen storage dynamics. In: *2016-01-0971, SAE 2016 world congress and exhibition*, Detroit, MI, 12–14 April 2016.
33. Muske KR, Jones JCP and Franceschi E. Adaptive analytical model-based control for SI engine air–fuel ratio. *IEEE Trans Control Syst Technol* 2008; 16(4): 763–768.
34. Chen AS, Na J, Herrmann G, et al. Adaptive air-fuel ratio control for spark ignition engines with time-varying parameter estimation. In: *2017 9th international conference on modelling, identification and control (ICMIC)*, 2017, pp.1074–1079. New York: IEEE. [AQ: 14]